A LABORATORY MODEL FOR THE GENERAL OCEAN CIRCULATION

By D. J. BAKER, Jun. and A. R. ROBINSON
Pierce Hall, Harvard University, U.S.A.

(*Communicated by S. Goldstein, F.R.S.—Received* 11 *November* 1968)

[Plates 12 to 16]

CONTENTS

A laboratory model for the study of a barotropic general ocean circulation has been constructed following the strict geometrical constraints of the β-plane approximation. Fluid is confined by plastic blocks to the volume defined by the intersection of two spherical surfaces, of common centre and slightly different radii with a circular cylinder whose axis intersects the centre of the spheres. The entire system is rotated and an interior circulation is provided by relative rotation of one of the bounding blocks. Uniform density of the rigidly enclosed fluid ensures the irrelevance of laboratory gravity and the absence of centrifugal effects on the flow. Fluid flow is observed with an electrochemical technique. Lines of coloured fluid which move with the local velocity are produced and photographed; velocities are inferred to 5% accuracy. Rossby numbers from 1.3×10^{-4} to 7.7 and Ekman numbers from 3.1×10^{-4} to 3.1×10^{-2} have been achieved. The apparatus can be oriented at an arbitrary mean latitude. The phenomena characteristic of linear subtropical gyres have been observed: a meridional Sverdrup flow, its associated zonal flow and a western boundary current. The existence, structure, and parameter dependencies of these features are in good agreement with the predictions of a general linear boundary layer analysis which has been developed for a thin barotropic ocean. The Sverdrup vorticity balance and the width and structure of the bottom frictional western boundary current have been established within the experimental uncertainties. In the nonlinear régime the position of the centre of the gyre has been measured as it migrates north-westward;

Vol. 265. A. 1168. (Price £1. 6s.; U.S. $3.40) 56 [Published 31 December 1969

a poleward eastern boundary current appears. These results agree with theoretical estimates for the onset of nonlinear behaviour. A long period time dependent flow is observed for high Rossby number. Quantitative studies have been made on an equatorial undercurrent which moves in a direction opposite to the surface forcing velocity. For low Rossby numbers this flow reverses with change in direction of the forcing velocity. In the nonlinear régime, the westward flowing undercurrent developed a streakiness and disappeared; whereas the eastward flowing current remained defined and measurable.

1. THE PROBLEM AND THE MODEL

1.1. *The general circulation problem*

To understand the physics of the general circulation of the oceans remains a challenging problem in planetary scale fluid dynamics. Although certain qualitative aspects of the distribution of currents have been rationalized, the fundamental manner in which momentum, vorticity and energy are conserved in the circulation remains unknown. This complex problem will be unravelled only through simultaneous attack by empirical observational studies, the examination of such data via heuristic mathematical models, and the probing of relevant fluid dynamical process via experimental and theoretical models. In the latter category falls a number of recent studies of the so-called wind driven ocean circulation problem, i.e. the problem of relating the distribution of surface or depth averaged currents to the distribution of surface wind stress. (Robinson 1965; Stommel 1965; Greenspan 1968.)

Early studies were successful in relating gross features of the circulation to the wind forcing in terms of very simple linear mathematical models which included the gross constraints of the Earth's rotation and geometry. The geometry is approximated by local surface Cartesian coordinates and Coriolis accelerations are effected only by the vertical component of the Earth's rotation, which varies with latitude (the β-plane). Central to these models is a simple balance of vorticity which is characteristic of the vast regions of the subtropical oceans away from continental boundaries and the equator (the Sverdrup vorticity relation). The relation arises from an approximate horizontal momentum balance which is geostrophic below a surface boundary layer through which the surface stress is imparted to the deeper fluid. This relation, when integrated over depth, relates the local meridional transport to the wind stress curl, and in this form has been subject to some direct observational verification (see, for example, Wyrtki 1964). It may be concluded that these terms contribute significantly to the mid-ocean balance. Further support for the Sverdrup balance accrues from the order of magnitude agreement between simple theory and observation of the transports of western boundary currents.

The existence of the major subtropical gyres is implied by the Sverdrup relation since these regions are isolated (in the transport sense) from the rest of the world ocean by approximate latitudes of zero wind stress curl. The Sverdrup relation further implies that such a closed circulation must somewhere have a more complex vorticity balance. In simple dissipative models the deviation occurs near the western boundary, thus accounting for the Gulf Stream phenomenon as a mass conserving planetary boundary layer.

However, more realistic models must include the nonlinear process of momentum advection in at least some part of the non-Sverdrup flow. The inclusion of these terms increases the difficulty of the problem enormously, and although a good deal of work (analytical and numerical) has been done in attempting to understand this process, very little real progress has been made in understanding the general circulation. Even the simplest general circulation models that contain the nonlinear process lead to very complex mathematics which has not been able to be

resolved unambiguously even through numerical analysis. The procedure of deducing a two-dimensional system which is possible in the linear models by an integration over depth is precluded by nonlinearities. Although a number of nonlinear studies have been done with a heuristic two-dimensional analogue problem, it is not clear to what extent the resulting flow patterns are representative of any actual physical system. Furthermore, in the attempt to keep the models as simple as possible the possibility of critical comparison with the circulation of real oceans has been lost.

1.2. *The role of laboratory experiments*

Our understanding of the general ocean circulation can be enhanced by a laboratory model by which the kind of theory applied to the real ocean, cast in specific terms for the experiment, is subject to critical test. The effects of approximations made in analytical theories, both in the initial assumptions and the subsequent solutions of equations, can be checked quantitatively. Insight into the relevance of numerical models and approximations as applied to the ocean can also be gained by similar numerical experiments on the laboratory model. The results of this interplay between laboratory model, analytic and numerical theory may then be used to guide a renewed attack on the real ocean problem, which in turn may lead to new laboratory experimentation. As well as elucidating partially explored phenomena in a controlled situation (the role of nonlinear boundary currents), a laboratory model may serve as a source of new oceanic phenomena (time dependent forcing). A well designed model experiment should raise more questions about the behaviour of both controlled and natural fluids than it answers.

The careful design of a laboratory experiment can enhance its usefulness as a guide towards understanding of geophysical problems. The design should be based upon all available knowledge of the phenomenon examined in a non-dimensional framework. The process to be explored is then isolable by a similarity matching in the appropriate parameters, with an awareness of the parameters which are either of negligible importance or deliberately altered or ignored. The necessary descriptive parameters arise from theoretical considerations; observation reveals the relevant ranges of values. Although a laboratory experiment may form an interesting physical system in its own right, its usefulness in geophysics is enhanced through proper design. The proper design must be followed by quantitative studies, in order that critical tests may unambiguously verify or reject theory. The combination of quantitative measurements with a careful and imaginative search for new phenomena exploits a properly designed experiment, and yields thereby the most profound insight into the geophysical process.

The experiment to be described below is a barotropic general ocean circulation model in which an interior vorticity balance of Sverdrup type serves as a basic design pivot. A quantitative demonstration of such β-plane geostrophy has been achieved in the model and the ageostrophy introduced by boundaries, friction and nonlinearities explored. The parameter ranges were chosen in order to provide for the linear theory an unambiguous and quantitative application, and to penetrate into the nonlinear régime.

1.3. *Process isolation and the model*

The parameters governing the design of the experiment derive from the scales and amplitude of the motion, and the geometry. The general circulation scale is here considered to mean that of the major oceanic subtropical gyres, which have similar features (Munk 1950, table 3). Thus the concept of a typical gyre is useful in model making. The vertical scales of the motion are overall determined by the morphology of the ocean basins and by gravity, which produces an

essentially spherical equipotential surface.† The motion is known to be approximately geostrophic and hydrostatic, the latter constraint resulting primarily from the extreme thinness of the ocean.

The geometry of the gyres may be idealized to that of a thin partial spherical shell. In a homogeneous model of the ocean, the spherical shape of the upper surface can be modelled mechanically by a rigid boundary. The rigid container may be rotated to produce Coriolis

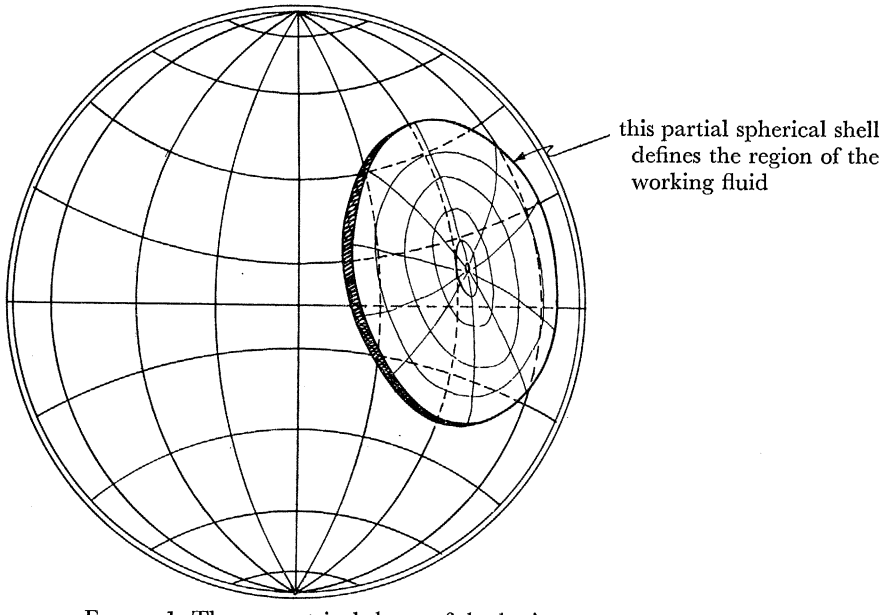

FIGURE 1. The geometrical shape of the basin.

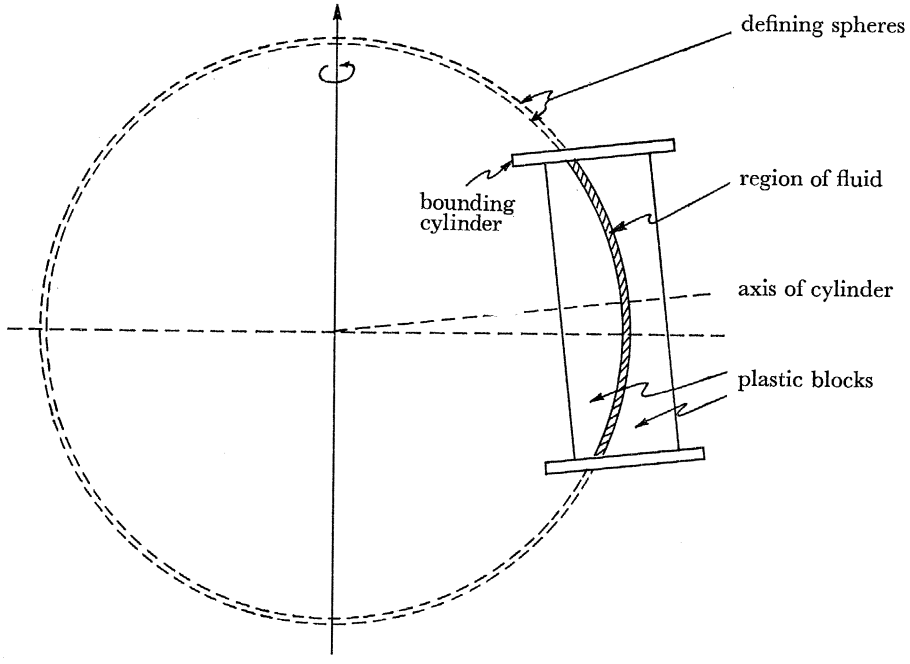

FIGURE 2. Defining spheres and cylinder.

† The distortion of the free surface due to centrifugal effects, normal pressure distributions, geostrophic motion, and the piling up of water due to tangential wind stresses, is of negligible importance.

accelerations. If the fluid be confined on all sides by rigid boundaries, the only effect of laboratory gravity (a conservative force) will be to join with the centripetal acceleration (also conservative) to modify the static pressure distribution. However, the dynamic pressure, and thus the velocities relative to the container will be unaffected by the static pressure distribution. Since radial gravity fields are not yet attainable in the laboratory it is not presently feasible to model the motion of a stratified fluid on a sphere.

We have constructed a model following the above general considerations and the detailed design criteria in the section to follow. The working fluid, water of homogeneous density, is confined to the shape of a thin spherical cap. Figure 1 illustrates this cap. A side view of the volume extracted from the defining spheres is depicted in figure 2. The volume is isolated by machined plastic blocks, which are set on a rotating turntable. Since the kinematic effect of the rotation is only to produce Coriolis accelerations, the position of the axis of rotation is arbitrary; the most convenient position for it in this experiment is through the centre of the working fluid. The relative rotation of either or both of the blocks forms a convenient source of momentum flux; the fluid motions are thus forced by a surface velocity of constant curl. In order to view the flow without obstruction, the bottom block rotates while the upper one remains stationary. Thus our ocean is upside down, which is irrelevant for dynamic modelling.

2. The design criteria

2.1. *Derivation of the β-plane equations*

It has been shown (Robinson 1965) that the β-plane equations are derivable from the spherical equations by purely geometrical considerations. This is done by neglecting only terms small in the geometrical parameters within groups of terms of like dynamical origin. Thus, the approximate β-plane equations contain a full set of non-dimensional parameters upon which an analysis of the dynamics of any flow to occur in the container can be based. The derivation is recapitulated here with a more complete treatment of the vertical equation and with a specialization to molecular frictional terms, relevant for a laboratory experiment.

Let R, θ, ψ be spherical coordinates (positive respectively in the radial (vertical†), latitudinal (northward), and longitudinal (eastward) directions, with w, v, u the corresponding velocities relative to a sphere rotating with angular velocity Ω. The momentum and continuity equations are

$$\frac{\partial u}{\partial t}+w\frac{\partial u}{\partial R}+\frac{v}{R}\frac{\partial u}{\partial \theta}+\frac{u}{R\cos\theta}\frac{\partial u}{\partial \psi}+\frac{wu}{R}+\frac{vu}{R}\tan\theta+2\Omega\,(w\cos\theta-v\sin\theta)$$
$$=-\frac{1}{\rho R\cos\theta}\frac{\partial p}{\partial \psi}+\nu\left(\nabla^2 u-\frac{u}{R^2\cos^2\theta}+\frac{2}{R^2\cos\theta}\frac{\partial w}{\partial \psi}+\frac{2\sin\theta}{R^2\cos^2\theta}\frac{\partial v}{\partial \psi}\right), \tag{2.1}$$

$$\frac{\partial v}{\partial t}+w\frac{\partial v}{\partial R}+\frac{v}{R}\frac{\partial v}{\partial \theta}+\frac{u}{R\cos\theta}\frac{\partial v}{\partial \psi}+\frac{wv}{R}-\frac{u^2\tan\theta}{R}+2\Omega u\sin\theta$$
$$=-\frac{1}{\rho R}\frac{\partial p}{\partial \theta}+\nu\left(\nabla^2 v+\frac{2}{R^2}\frac{\partial w}{\partial \theta}-\frac{v}{R^2\cos^2\theta}-\frac{2\sin\theta}{R^2\cos^2\theta}\frac{\partial u}{\partial \psi}\right), \tag{2.2}$$

$$\frac{\partial w}{\partial t}+w\frac{\partial w}{\partial R}+\frac{v}{R}\frac{\partial w}{\partial \theta}+\frac{u}{R\cos\theta}\frac{\partial w}{\partial \psi}-\frac{u^2+v^2}{R}-2\Omega u\cos\theta$$
$$=-\frac{1}{\rho}\frac{\partial p}{\partial R}+\nu\left(\nabla^2 w-\frac{2w}{R^2}-\frac{2}{R^2}\frac{\partial v}{\partial \theta}-\frac{2v\tan\theta}{R^2}-\frac{2}{R^2\cos\theta}\frac{\partial u}{\partial \psi}\right), \tag{2.3}$$

† By convention for modelling; similarly the other two components will be referred to as horizontal. A list of symbols employed in the text appears at the end of the paper.

$$\frac{1}{R^2}\frac{\partial}{\partial R}(R^2 w) + \frac{1}{R\cos\theta}\frac{\partial}{\partial\theta}(v\cos\theta) + \frac{1}{R\cos\theta}\frac{\partial u}{\partial\psi} = 0, \tag{2.4}$$

where ν is the kinematic viscosity, ρ the (homogeneous) density, and p the difference of the pressure from its hydrostatic value which balances the gravitational and centripetal potential.

The fluid is confined within the volume defined by the intersection of two spherical surfaces, of common centre and of radii R_0, $R_0 + H$, with a circular cylinder whose axis intersects the centre of the spheres and lies somewhere on the cone of angle $\frac{1}{2}\pi - \theta_0$ from the axis of rotation. The spherical circle cut from the inner sphere by the cylinder is of diameter $2L$.

Let a set of surface coordinates be defined by

$$z = R - R_0, \quad y = R_0(\theta - \theta_0), \quad x = R_0\cos\theta_0\psi,$$

or the equivalent cylindrical coordinates r, ϕ, z (see figure 3). Let non-dimensional independent and dependent variables be defined by

$$\begin{aligned} x &= Lx' & u &= \omega L u', \\ y &= Ly', & v &= \omega L v', \\ z &= Hz', & w &= (H/L)\,\omega L w', \\ t &= \frac{t'}{\tau} & p &= \frac{2\Omega\omega L^3\rho\cos\theta_0}{R_0}p', \end{aligned}$$

The horizontal velocities are non-dimensionalized by the relative angular velocity ω of the lower rotating surface. The scale of the vertical velocity has been chosen H/L smaller, so as to upper bound the vertical mass flux divergence by the horizontal divergence.

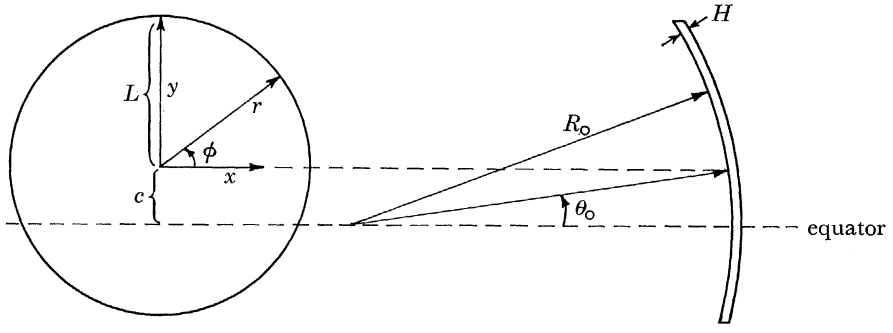

FIGURE 3. Coordinate system.

Subtropical gyres are characterized by the geometrical constraints

$$(L/R_0)^2 \ll 1, \quad (L/R_0)\tan\theta_0 \ll 1, \quad H/R_0 \ll 1, \quad HR_0/L^2 \ll 1. \tag{2.5}$$

Under application of all but the last of (2.5), equations (2.1 to 2.4) reduce to

$$\delta u_t - \gamma[u_{zz} + \lambda^2(u_{xx} + u_{yy})] + \epsilon[uu_x + vu_y + wu_z] - fv + Aw + p_x = 0, \tag{2.6}$$

$$\delta v_t - \gamma[v_{zz} + \lambda^2(v_{xx} + v_{yy})] + \epsilon[uv_x + vv_y + wv_z] + fu + p_y = 0, \tag{2.7}$$

$$\delta w_t - \gamma\lambda^2[w_{zz} + \lambda^2(w_{xx} + w_{yy})] + \lambda^2\epsilon\left[uw_x + vw_y + ww_z + \frac{1}{A}(u^2 + v^2)\right] + Au + p_z = 0, \tag{2.8}$$

$$u_x + v_y + w_z = 0. \tag{2.9}$$

Here (and henceforth) the primes are dropped from non-dimensional variables. The non-dimensional parameters are defined by

$$\left.\begin{aligned} \delta &\equiv \frac{\tau}{2\Omega\cos\theta_0}\left(\frac{R_0}{L}\right), & c &\equiv \frac{R_0}{L}\tan\theta_0; \\ \gamma &\equiv \frac{\nu R_0}{2\Omega\cos\theta_0 H^2 L}, & \lambda &\equiv \frac{H}{L}; \\ \epsilon &\equiv \frac{\omega R_0}{2\Omega\cos\theta_0 L}, & \Lambda &\equiv \frac{HR_0}{L^2}. \end{aligned}\right\} \tag{2.10}$$

The Coriolis parameter, defined as $f \equiv c+y$, differs somewhat from the usual definition in order to include simply an equatorially centred gyre. The definitions (2.10) are thus based on the β-effect and not the usual laboratory Ω or planetary f_0 ($\equiv 2\Omega\sin\theta_0$).

2.2. *Parameter ranges*

The design characteristics for the laboratory model must reflect an acceptable compromise between oceanic gyre estimates, absolute scale constraints of the laboratory, certain stability considerations, and measurement feasibility.

Four geometrical parameters are involved: the depth of the shell (H), the radius of the circular basin (L), the radius of curvature of the sphere (R_0), and the latitude of the centre of the basin (θ_0). Typical values which characterize the North Atlantic Ocean between 15 and 50° N (average latitudes of zero wind stress curl) are $H = 4\times10^5$ cm, $L = 2\times10^8$ cm, $R_0 = 6.4\times10^8$ cm and $\theta_0 = 30°$. Thus the ratios

$$H/R_0 \cong 6\times10^{-4}, \qquad (L/R_0)^2 \cong 0.1,$$
$$HR_0/L^2 \cong 6\times10^{-3}, \quad (L/R_0)\tan\theta_0 \cong 0.2,$$

more precisely replace the inequalities (2.5) for this gyre. The relevance of a model experiment to the β-plane can be measured by the closeness to which it adheres to these restrictions. Most difficulty occurs in achieving sufficiently small Λ, the crucial restraint on the modelling of thin rotating subtropical oceans.

The existence and stability of Ekman boundary layers near the horizontal surfaces lead to restrictions on the total depth (H). The e-folding scale of these layers at latitude θ_0 is given by $(\nu/\Omega\sin\theta_0)^{\frac{1}{2}}$, which depth must be small compared to the total depth of the shell. A reasonable criterion is

$$H \gg 3\left(\frac{\nu}{\Omega\sin\theta_0}\right)^{\frac{1}{2}}.$$

From the available rotation rates (see table 2) and the viscosity of the working fluid (chosen to be water from flow visualization consideration), $H \gg 0.15$ cm. The choice $H = 1$ cm satisfies this criterion, is large enough to allow placement of fluid flow markers, and is still small enough to allow reasonable choices of R_0, L and θ_0.

Recent studies (Faller 1963; Tatro & Mollo-Christensen 1967) have shown that, if Re be defined as a Reynolds number based on the geostrophic velocity and the Ekman layer thickness, and if Ro be defined as a Rossby number based on the ratio of the relative inertial acceleration to the Coriolis acceleration, instability of the Ekman layer occurs for values of $Re > (56.3 + 116.8\,Ro)$. The f-plane geometry and source sink arrangement of their experiments produce comparable amplitudes of the geostrophic and Ekman layer velocities. In the β-plane geometry, over most

of the flow the Ekman layer velocities, comparable to the surface forcing velocity, are an order of magnitude larger than the geostrophic velocities. Thus, to use their results to indicate the probable stable range for β-plane geometry, the onset of instability is estimated here with typical Ekman layer velocities. In the western boundary current region the geostrophic flow is comparable to the surface velocity, thus the criterion is more directly applicable. The above criterion indicates that the Ekman layers will be stable if the forcing angular velocity is less than $0.8\,\mathrm{rad\,s^{-1}}$ (assuming typical values of the other parameters). Most of the quantitative mid-latitude measurements in this paper fall into the stable region, although the largest nonlinear western boundary current velocities were not measurable with the present techniques and thus may exhibit unstable Ekman layers. For the more rapid relative rotations the larger Reynolds number produced by equatorial thickening of the Ekman layers indicates possible instability (especially near the rim). However, the application of this criterion there is obviously suspect; no such instability was apparent, but the exploration was incomplete.

The scale of L was chosen as 20 cm, the largest spherical shape that could be cut by the curve tracing lathe readily available. With H and L determined, $R_0 = 53.5\,\mathrm{cm}$ and $\theta_0 = 31.4°$ were chosen to yield the best compromise to the geometrical restrictions for the modelling of the subtropical gyre. The results are summarized in table 1. (The parameter λ is also included for later reference, although the assumption that it is small is not independent of (2.5).) In the apparatus developed, L, R_0 are fixed and H, θ_0 variable.

TABLE 1. GEOMETRICAL PARAMETERS

parameter	theory	laboratory experiment	typical oceanic gyre
H/R_0	$\ll 1$	0.0187	0.00063
$(L/R_0)^2$	$\ll 1$	0.144	0.098
$(L/R_0)\tan\theta_0$	$\ll 1$	0.231	0.18
$HR_0/L^2\,(\equiv \Lambda)$	$\ll 1$	0.130	0.0064
$H/L\,(\equiv \lambda)$	$\ll 1$	0.0493	0.0020

The choice of relevant range of values for the frictional parameter γ presents some difficulty because of the dubiety and ambiguity inherent in characterizing oceanic flows by one or even several frictional parameters. Coefficients of eddy viscosity inferred from oceanic measurements range from 1 to $10^4\,\mathrm{cm^2\,s^{-1}}$ (vertical) and 10^6 to $10^8\,\mathrm{cm^2\,s^{-1}}$ (horizontal) (Sverdrup, Johnson & Fleming 1942, tables 65 and 66). Values of γ may be estimated by making γ and $\gamma\lambda^2$ respectively similar to the vertical and horizontal non-dimensional frictional parameters for the ocean. There results for γ the range 10^{-2} to 10^{-6} (vertical), 10^{-1} to 10^{-3} (horizontal). Most uncertainty lies in the horizontal coefficient, indeed negative values have been suggested (Webster 1965). The laboratory frictional parameter is, of course, determined by the molecular viscosity, and is well known.

The parameter ϵ is an overall Rossby number and it may be estimated by using observed surface velocities. Over a typical gyre the velocities may range from 1 to $300\,\mathrm{cm\,s^{-1}}$. These values indicate that ϵ will have a minimum of about 5×10^{-5} and may go as high as 0.1 in a (nonlinear) western boundary current.

Pilot studies of time dependent flow have been performed, basing estimates of δ on the theoretical values of τ for the free modes of an enclosed basin. These studies will not be reported here, but we intend to pursue them together with an investigation of forced transient circulation.

The model has been designed to include the above parameter ranges as closely as possible, and also to provide for the exploration of the circulation in parameter space, from the strictly linear régime to well into nonlinear régimes of flow. In summary, the quantities ν, L, R_0, are fixed, H, θ_0, ω and Ω are variable. Table 2 indicates the ranges of these quantities. Table 3 indicates the range of the parameters ϵ, γ, λ and Λ which can be achieved for the laboratory experiment and presents a comparison with the values of the parameters as estimated for the ocean. The available range clearly permits a study of the oceanic circulation in the proper range of Ekman and Rossby numbers, with reasonably similar geometry. The parameters γ and ϵ become ∞ when $\Omega = 0$; the upper bounds to these parameters in table 3 are for the lowest values of Ω such that Ekman layers are only 20 % of the total depth.

TABLE 2. RANGE OF EXPERIMENTAL VARIABLES

variable	possible range (present equipment)	range used in present experiment
ν	$0.01\ \mathrm{cm^2\,s^{-1}}$	$0.01\ \mathrm{cm^2\,s^{-1}}$
R_0	53.5 cm	53.5 cm
L	20.3 cm	20.3 cm
H	0.5–4 cm	1.0 cm
θ_0	0–90°	0–31.4°
ω	$0.001–10\ \mathrm{rad\,s^{-1}}$†	$0–0.85\ \mathrm{rad\,s^{-1}}$
Ω	$2.0–40\ \mathrm{rad\,s^{-1}}$‡	$0–10\ \mathrm{rad\,s^{-1}}$

† The lower limit is fixed by the stability of the drive.
‡ The lower limit is fixed by the criterion that the Ekman layers be thin compared to the depth for $H = 1$ cm.

TABLE 3. RANGE OF NON-DIMENSIONAL PARAMETERS

parameters	$10^3 \times$ estimated oceanic range	$10^3 \times$ available model range
λ	2.0	75–9.4
Λ	6.4	520–65
ϵ	39–0.13	7700–0.13
γ	270–0.0017	31–0.33

3. THE EXPERIMENTAL APPARATUS AND TECHNIQUE

3.1. *The apparatus*

An apparatus possessing the above geometrical properties has been constructed from two machined lucite blocks and a lucite cylinder. The convex and concave surfaces were machined using a curve tracing lathe and then polished. The shape is axially symmetric about the axis of the bounding cylinder to better than 2 μm, but the variation in radius of curvature may amount to as much as 20 μm. However, this variation is small compared to typical Ekman boundary layer thicknesses in the experiment. Detailed front and side views of the apparatus are presented in figures 4 and 5. The upper and lower bounding blocks are designed to rotate independently of one another; however, in most of the studies presented here, the rotatable upper block has been replaced by a stationary one, as illustrated, and the circulation produced solely by the relative rotation of the lower surface. The region of the working fluid will be referred to as the (ocean) basin.

A sliding fit was made between the bottom rotating block and the outer bounding cylinder. The region which is filled with working fluid is indicated in figure 5. The thickness of the gap

between the block and the cylinder was 0.25 mm and qualitative observation indicated that the fluid showed no tendency to flow through. The driving motor for the bottom plate is a Bodine d.c. motor mounted on the rotating table and driven from the outside through the table slip rings by a Minarik Feedback control. This arrangement allows easy change of relative velocities from outside the rotating table. The angular velocities are steady to 0.1 %.

The rotating table upon which the entire apparatus is mounted was constructed at Harvard from a design kindly made available to us by D. Fultz (1965). The table is driven with a

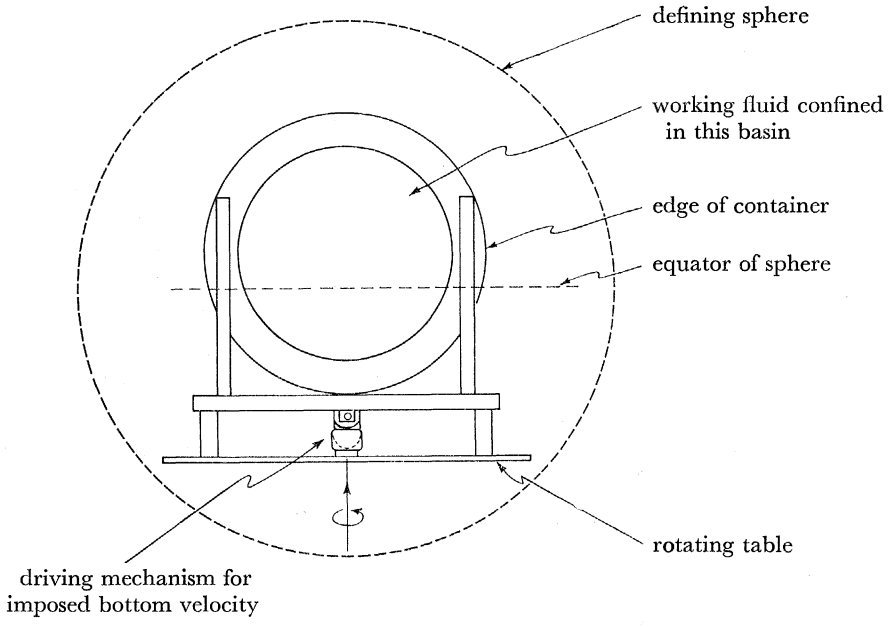

FIGURE 4. Sketch of front view of apparatus.

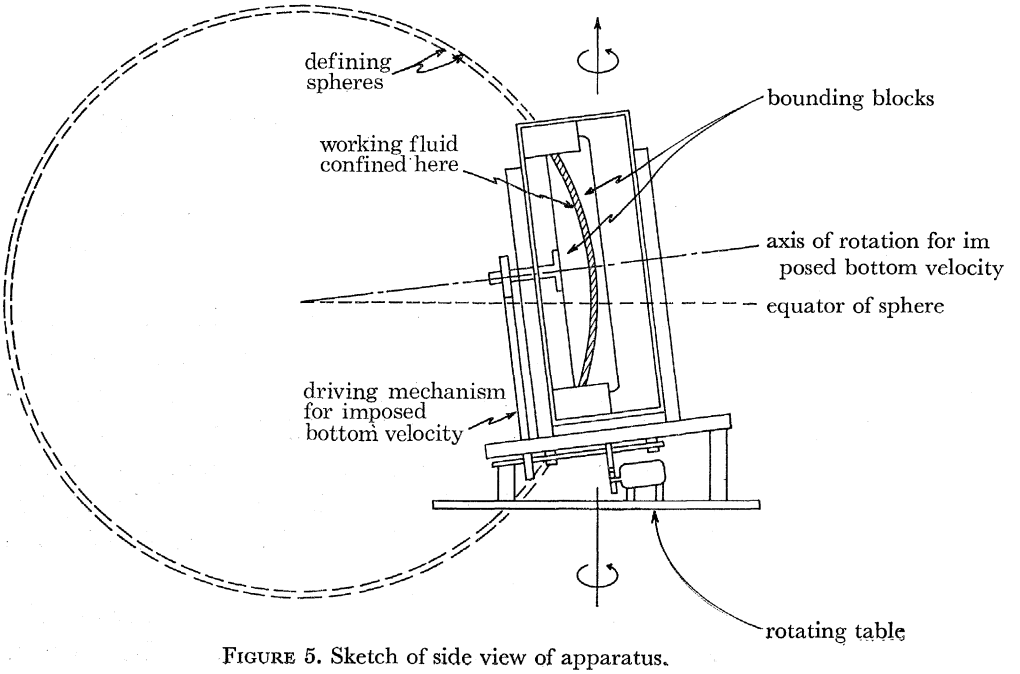

FIGURE 5. Sketch of side view of apparatus.

synchronous motor by a timing belt through a speed reducer and a Graham Transmission (Model 230 MR 2.8). The angular velocity of the table is measured by a digital tachometer (Hewlett–Packard Model 508 A) and a counter (Hewlett–Packard Model 5214 L). The angular velocity of the table is measured by averaging the number of counts over several 10 s periods ($\pm$ 0.2 % accuracy). Photographs of the apparatus mounted on the table are presented in figure 6.

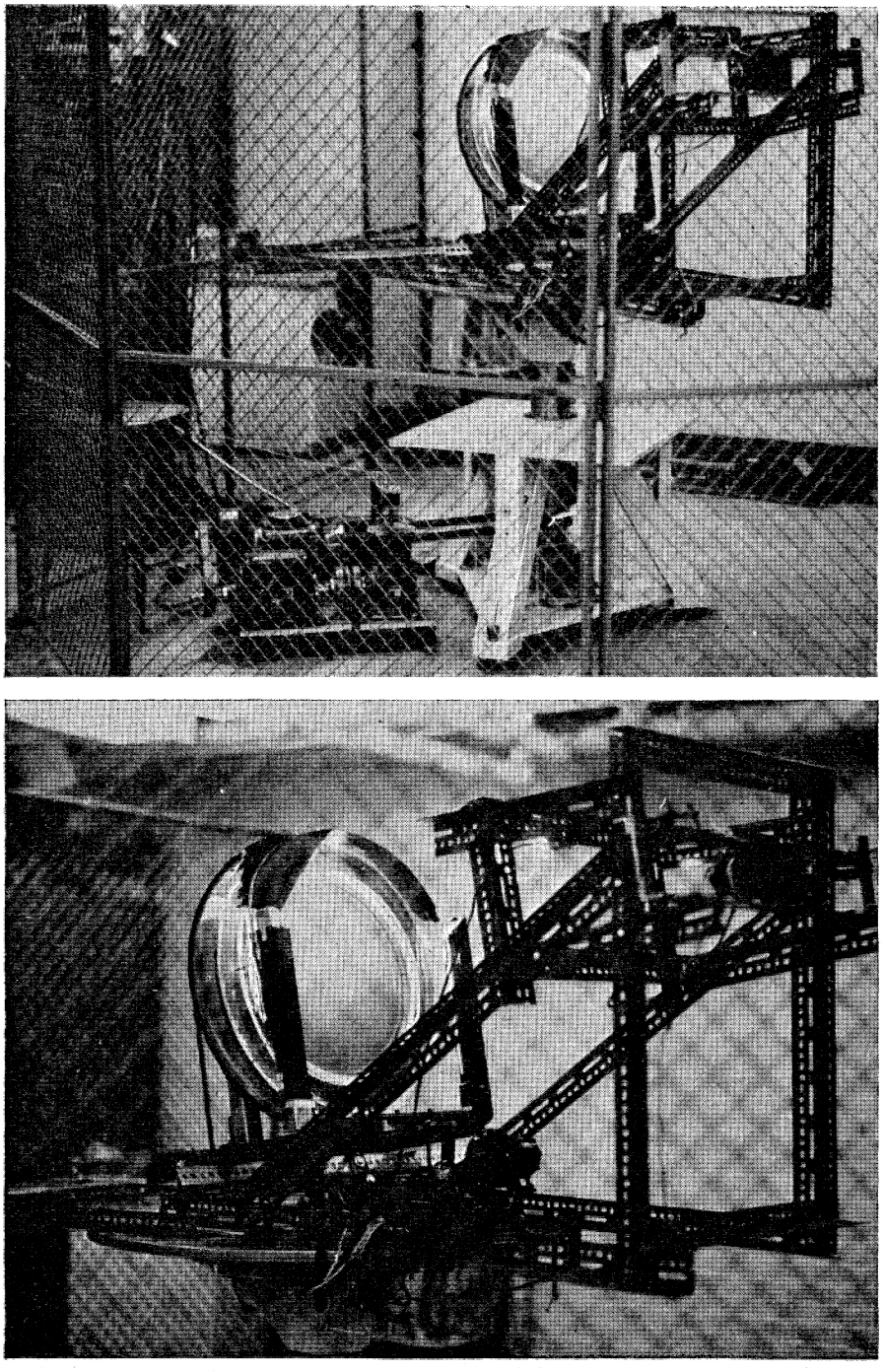

FIGURE 6. Above: the experimental apparatus, rotating table and drive mechanism. Below: the apparatus, relative drive mechanism (lower centre) and motorized camera (upper right).

In order to facilitate the fluid flow measurement, the curved surface of the lower cap has been painted white and a polar coordinate system marked on it for a background. This system consists of concentric circles with radii differing by 1.27 cm crossed by radial lines every 9°. The angular speed of the cap is measured by observing the time for a 90° sector to pass a non-rotating mark. The repeatability of this measurement was found to be about 3 %.

3.2. *Measurement of the flow*

A Lagrangian technique is used to delineate the flow field. Lines of marked fluid are produced by the following technique (Baker 1966): a grid of fine wires is placed in a 0.04 % aqueous solution of the pH indicator Thymol Blue, which has been titrated to the end point from the basic side. A second set of wires in the fluid completes a circuit in which an electrical current is allowed to flow. The resulting proton transfer reaction at the surface of the wire changes the pH and thus the colour of the solution locally. This coloured fluid moves with the local velocity. As the indicator is at all times in solution, the coloured fluid is precisely neutrally buoyant and undesired centrifugal effects are absent. The chemical technique is not useful for velocities greater than 3 or 4 cm s^{-1}, since the faster velocities sweep the coloured fluid away from the wires too rapidly for sufficient colour change to permit photography.

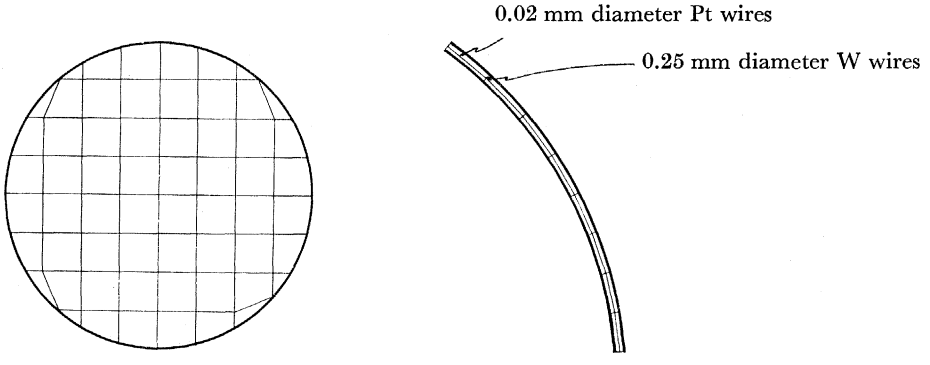

FIGURE 7. Front view and cross-section of wire grid measuring system.

The details of the grid (formed from 0.02 mm diameter platinum) are shown in figure 7. One grid of wires is glued to the surface of the upper block to serve as the electrode system; the second grid is placed midway between the two spherical surfaces, stretched between 0.25 mm diameter tungsten wires which have been heated and pushed into the plastic. The grid wires are sufficiently thin to have negligible effect on the flow. Although the thinnest possible wires are used for the rigid supports, some perturbation (demonstrably local) is evident. An estimation of this effect may be made using known results (Lamb 1932) of the effect of a cylinder on a uniform flow. These estimates indicate that the perturbations may be neglected compared to other experimental uncertainties in the region where the velocities are measured. As the platinum wire is stretched from post to post, the grid is not strictly spherical. However, the deviations from sphericity are not critical for measurement of linear geostrophic flow, since this flow does not vary in the local vertical direction.

An electrical current of 0.1 A through the circuit was required to produce sufficient colour change for photography. Although short (< 1 s) pulses of the current produced no noticeable convection effects due to heating, longer pulses of larger current did. All measurements were checked to show that convection effects were negligible by pulsing the circuit while the fluid

was in rigid body motion (zero relative driving). The necessary lighting for photography was found not to produce adverse convection effects.

Photographs of the flow were taken by a remote control 35 mm Nikon F camera with a motorized back, mounted on the table. This enabled sequential photographs, timed by a stopwatch, to be taken after the current pulse. The camera is mounted so that its focal plane is parallel to the tangent plane to the defining spheres at the centre of the basin; parallax effects were found to be negligible. Kodak Tri-x film was developed in Acufine developer and printed on Agfa BEH 1 grade 6 paper for maximum speed and contrast. Remote control motion pictures of the flow have proven useful primarily for qualitative studies particularly of time dependent effects. The poor resolution of readily available motion picture film has precluded quantitative measurements to date.

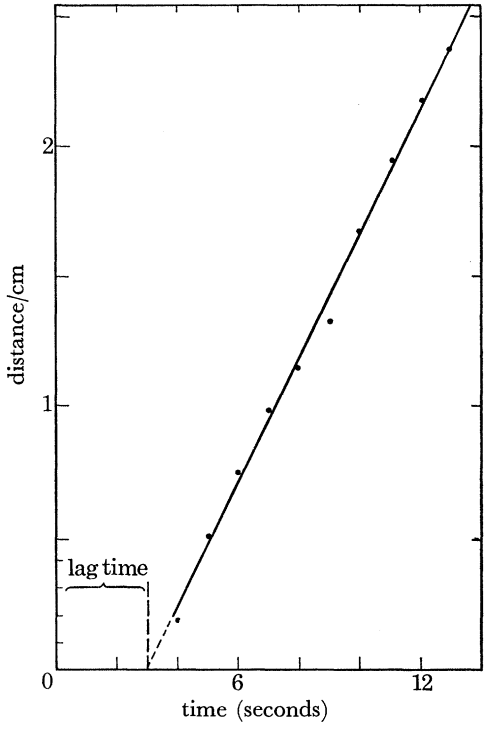

FIGURE 8. Displacement of marked fluid as a function of time after current pulse.

The procedure adopted for variation of the forcing relative angular velocity with fixed main rotation rate was as follows: relative angular velocity was measured with $\Omega = 0$, then the apparatus was brought to full speed, and a time corresponding to several spin-up times allowed to elapse before the sequential photographs were taken. Then the table was stopped, the relative angular velocity measured again, and the procedure repeated for a new relative angular velocity. A typical spin-up time (the e-folding time for the velocity field to reach its equilibrium state) is 6 s, and about 20 spin-up times were allowed to elapse in order to insure steady flow. A similar procedure was followed for the study of the dependence of the circulation on the main rotation rate.

3.3. *The treatment of the data*

Flow velocities are inferred from the photographs by obtaining the asymptotic slope of the curve which measures the distance a given part of the coloured fluid moves in time. The distances were measured from the photographs by a travelling microscope and are accurate to ± 0.5 mm.

This represents an uncertainty in the velocity of about 5 %. The major part of this uncertainty lies in the difficulty of determining the exact leading edge of the line of coloured fluid. Minor uncertainties introduced by unequal shrinking of the photographic paper during development are less than 1 %.

To obtain the velocity it is necessary to use the asymptotic slope of the distance–time curve because the chemical technique exhibits a lag time, i.e. the plot of distance against time is not linear near zero, but generally does have a linear asymptote (see figure 8). Over the distance in which sequential measurements were taken (< 1 cm) the variation of the velocity field was always small enough ($< 1\%$) so that the velocity could be considered uniform. The asymptotic slope is presented as the velocity at the centre of this distance for comparison with theory. Four sequential photographs were taken at each set of parameters. The slopes were obtained either by averaging various sets of two points or by plotting all the points, and again a 5 % accuracy was consistently indicated.

All of the quantitative measurements to be presented here were made at the grid placed midway between the two spherical surfaces. The technical difficulty of placing more than one set of grids between the spherical caps has precluded the possibility of obtaining the detailed vertical structure of the flow, although some visual observations were made with three wires in the vertical.

4. Summary of experimental results

In this section a brief qualitative description of the experimental results obtained to date is presented. Figure 9 is a photograph of the basin taken 24 s after the current was pulsed, and the general features of a linear subtropical gyre are evident. The relevant parameters are displayed on the figure. For this latitude ($\theta_0 = 31.4°$) the equator lies well below the basin. The sense of the forcing angular velocity is clockwise as viewed from the front and the main rotation counter-clockwise viewed from above.

A general southward drift ($\sim 0.4\,\mathrm{mm\,s^{-1}}$—the geostrophic Sverdrup flow) occurs in the central region. A zonal flow, eastward in the northern portion of the basin, westward in the southern, is of comparable speed and appears to be almost symmetric about the central latitude. A strong western boundary current occupies about one-eighth of the total basin width. The details of these features are in good agreement with theory. No pronounced boundary currents are noticed at the northern and eastern edges of the basin. However, a current is observed near the southern boundary of the basin, flowing towards the east. The flow pattern reverses upon change of the sign of ω. The local effects of the posts on the flow can be observed (note the centre post, where several wires are joined together).

The next figure (figure 10, plate 12) illustrates the character of the flow as θ_0 is varied from 31.4 to 0°. The values of experimental parameters for each photograph are presented in the figure; experience indicates that the qualitative differences are due only to the change in latitude. The forcing velocity is clockwise for each picture. Note the appearance of an equatorial undercurrent moving west to east in the region of the equator for $\theta_0 = 16°$ and 6° 40′. The extra-equatorial features appear to blend smoothly with the equatorial flow. When the central latitude is 0°, two undercurrents appear, above and below the equator. The zonal component in each case is opposite to the small east–west component of the bottom forcing velocity; the zero of the zonal flow appears to be located on the equator. The meridional component of undercurrent is more southward than northward, but is generally opposite to the forcing velocity component. The

zonal flow appears symmetric, but the western boundary current moves smoothly across the equator. For small values of the forcing velocity, these flows, including the undercurrents, reverse with change in the sign of ω.

As the bottom forcing velocity is increased, qualitative changes appear in the flow patterns (see figure 11, plate 13). Subtropically, the most striking change is a migration of the centre of the gyre towards the northwest. The speed of the western boundary current increases until it is too fast to measure by the chemical technique. The intense flow continues around the circular boundary, and is visible as a current even in the northeast. The flow also exhibits some time dependence.

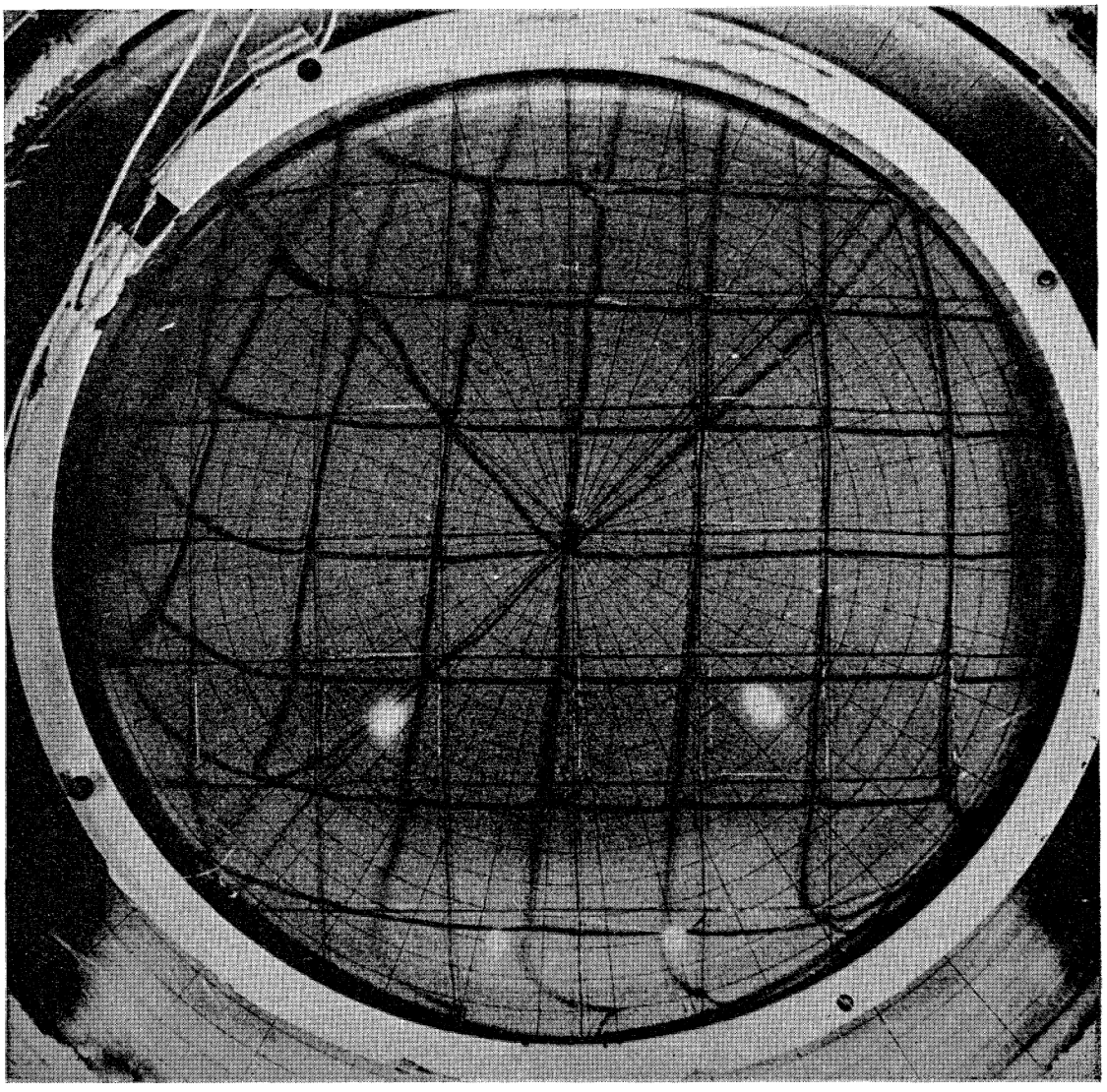

FIGURE 9. Position of ink lines 24 s after current pulse, illustrating general features of extra-equatorial flow. ($\theta_0 = 31.4°$, $\Omega = 6.31$ rad s^{-1}, $\omega = 0.0270$ rad s^{-1}, $\epsilon = 0.00661$, $\gamma = 0.00245$, $\gamma^{\frac{1}{2}} = 0.0495$.)

The most striking feature observed in the equatorial flow as the forcing velocity is increased is the disappearance of the westward flowing undercurrent (which does exist for smaller values of counterclockwise ω). Whether the current becomes unstable or is moving too fast to observe with

the chemical technique is moot. However, the westward undercurrent does disappear at an absolute value of forcing velocity for which the eastward undercurrent is stable and easily measurable. Widths and velocities as functions of the parameters have been measured and empirical formulae derived.

The effect on the flow pattern of varying main rotation rate is shown in figure 12, plate 13. Care must be exercised in the interpretation of this set of photographs, because of the varying ratio of γ/ϵ. The pattern is perfectly symmetric when $\Omega = 0$; the westward intensification develops and intensifies as Ω is increased. The Ekman layers are fully developed when $\Omega = 2$ rad s^{-1}. This is a striking illustration of the 'β-effect', since the flow between two flat disks remains, of course, symmetrical as Ω is increased from zero (Baker 1967).

5. THEORY OF THE LINEAR RÉGIME

Direct solution of even the linearized version of the governing equations and associated boundary conditions is too complex to accomplish directly. The theoretical analysis therefore invokes boundary layer and numerical techniques. The boundary layer analysis in the horizontal variables involves a careful consideration of the boundary conditions and the vertical structure of the flow, including the Ekman layers. The theory has been developed simultaneously with the experimental study, with profitable feedback.

The approximate analytical solution of equations (2.6 to 2.9) for steady flow ($\delta = 0$) involves simultaneous (ordinary and singular) perturbation expansions in the small parameters ϵ, λ, A, γ. The details of the circulation, e.g. even the simple mid-basin geostrophic flow, depend intimately on the relative size of these parameters. The discussion here will be descriptive rather than deductive; a more detailed treatment of the problem is given elsewhere (Robinson 1969) and should be referred to for amplification of what follows.

5.1. *The Sverdrup flow*

Away from the vicinity of the circular side boundary the linear flow is describable by Ekman layers at the upper and lower bounding surfaces and an interior geostrophic flow, characterized by the Sverdrup geostrophic vorticity balance $v = f\partial w/\partial z$. In equations (2.6 to 2.8) let $\lambda \ll 1$, $A \ll 1$ and $\epsilon \ll 1$, whence, with (2.9)

$$-\gamma u_{zz} - fv + p_x = 0, \tag{5.1}$$

$$-\gamma v_{zz} + fu + p_y = 0, \tag{5.2}$$

$$p_z = 0, \tag{5.3}$$

$$u_x + v_y + w_z = 0, \tag{5.4}$$

result, to be solved under the conditions,

$$\left.\begin{aligned} u(x,y,0) \equiv U_B = -\sigma y, \quad v(x,y,0) \equiv V_B = +\sigma x, \\ u(x,y,1) = v(x,y,1) = 0, \end{aligned}\right\} \tag{5.5}$$

for $\gamma \ll 1$. The sense of the lower boundary rotation is traced by $\sigma = \pm 1$ (counterclockwise $+$).

Equation (5.3) implies $p(x,y)$ only. Let $\zeta_0 = (f/2\gamma)^{\frac{1}{2}} z$ (near $z = 0$) and $\zeta_1 = (f/2\gamma)^{\frac{1}{2}}(z-1)$ (near $z = 1$). The velocities are separated into three parts, an interior and two boundary layer contributions. Let $u = u^G(x,y) + u^0(x,y,\zeta_0) + u^1(x,y,\zeta_1)$ and similarly for v and w, but $w^G = W(x,y) + \beta p_x z/f^2$ varies linearly in z. The horizontal functions p, W are governed by equations obtained upon explicit solution of the Ekman layer equations and satisfaction of all the conditions (5.5).

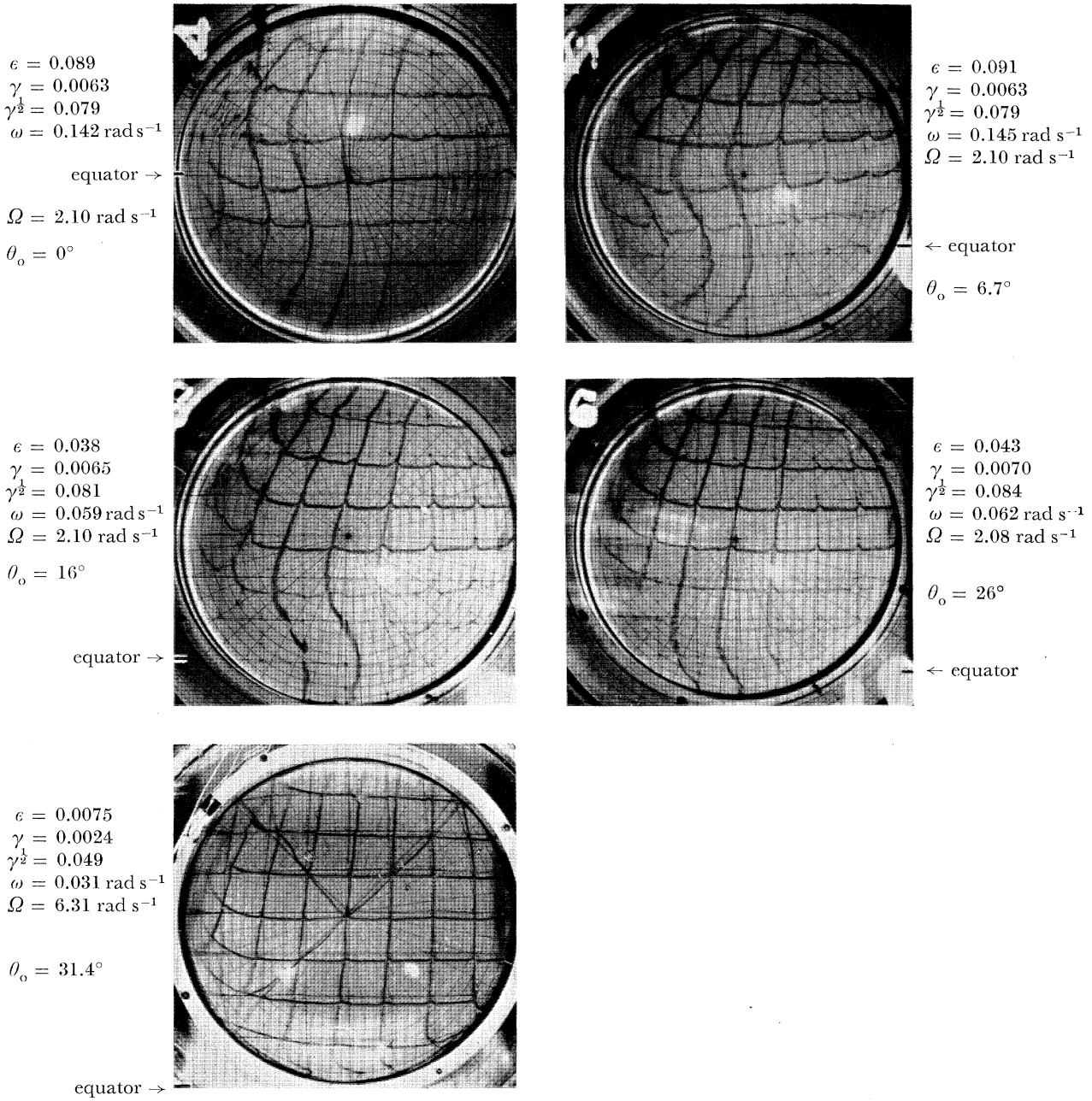

FIGURE 10. Variation in flow pattern as a function of θ_0. The equator and relevant data are indicated for each picture.

(*Facing p.* 548)

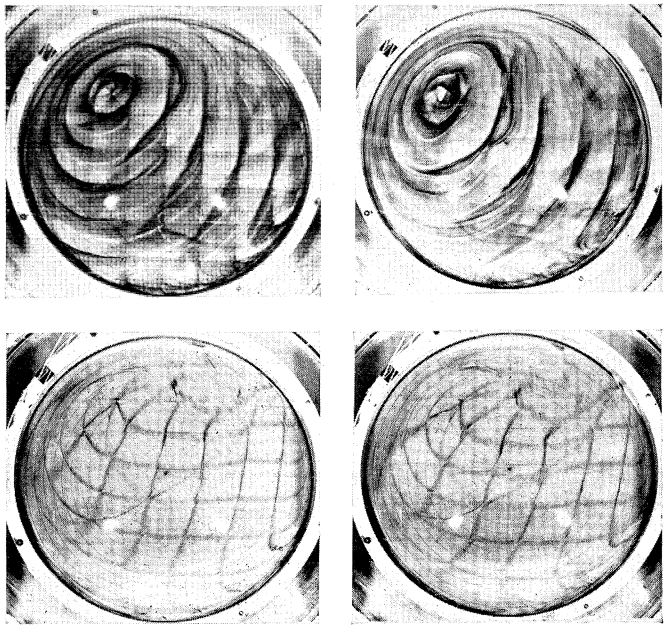

FIGURE 11. Photographs of flow for large ϵ. The right-hand photographs were taken 0.3 s after the left-hand ones. The upper pictures represent a continuous flow of dye; the lower, a pulse. ($\theta_0 = 31.4°$, $\Omega = 6.31$ rad s^{-1}, $\omega = 0.850$ rad s^{-1}, $\epsilon = 0.207$, $\gamma = 0.00245$, $\gamma^{\frac{1}{2}} = 0.0495$.)

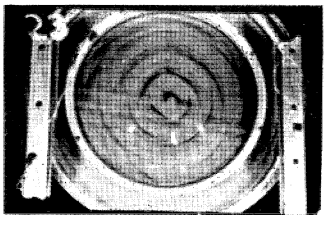

$\Omega = 0$ rad s^{-1}
$\gamma = \epsilon = \infty$

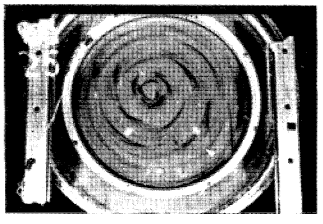

$\Omega = 0.261$ rad s^{-1}
$\gamma = 0.059$
$\gamma^{\frac{1}{2}} = 0.24$
$\epsilon = 0.94$

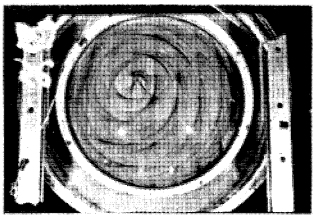

$\Omega = 0.512$ rad s^{-1}
$\gamma = 0.030$
$\gamma^{\frac{1}{2}} = 0.17$
$\epsilon = 0.48$

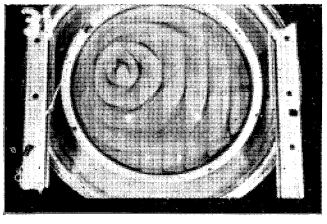

$\Omega = 2.23$ rad s^{-1}
$\gamma = 0.0069$
$\gamma^{\frac{1}{2}} = 0.0831$
$\epsilon = 0.11$

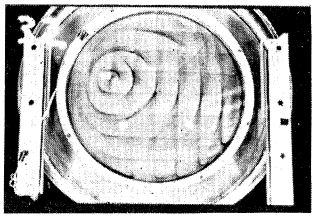

$\Omega = 3.17$ rad s^{-1}
$\gamma = 0.0049$
$\gamma^{\frac{1}{2}} = 0.070$
$\epsilon = 0.077$

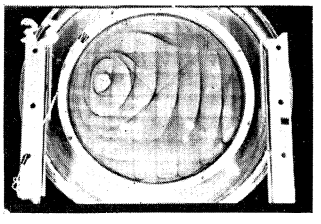

$\Omega = 4.15$ rad s^{-1}
$\gamma = 0.0037$
$\gamma^{\frac{1}{2}} = 0.061$
$\epsilon = 0.059$

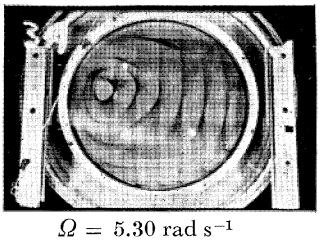

$\Omega = 5.30$ rad s^{-1}
$\gamma = 0.0029$
$\gamma^{\frac{1}{2}} = 0.054$
$\epsilon = 0.046$

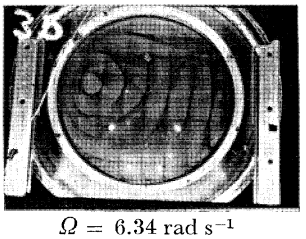

$\Omega = 6.34$ rad s^{-1}
$\gamma = 0.0024$
$\gamma^{\frac{1}{2}} = 0.049$
$\epsilon = 0.039$

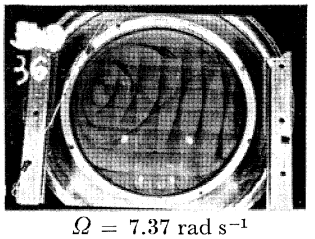

$\Omega = 7.37$ rad s^{-1}
$\gamma = 0.0021$
$\gamma^{\frac{1}{2}} = 0.046$
$\epsilon = 0.033$

FIGURE 12. Flow pattern as a function of Ω ($\theta_0 = 31.4°$, $\omega = 0.159$ rad s^{-1}).

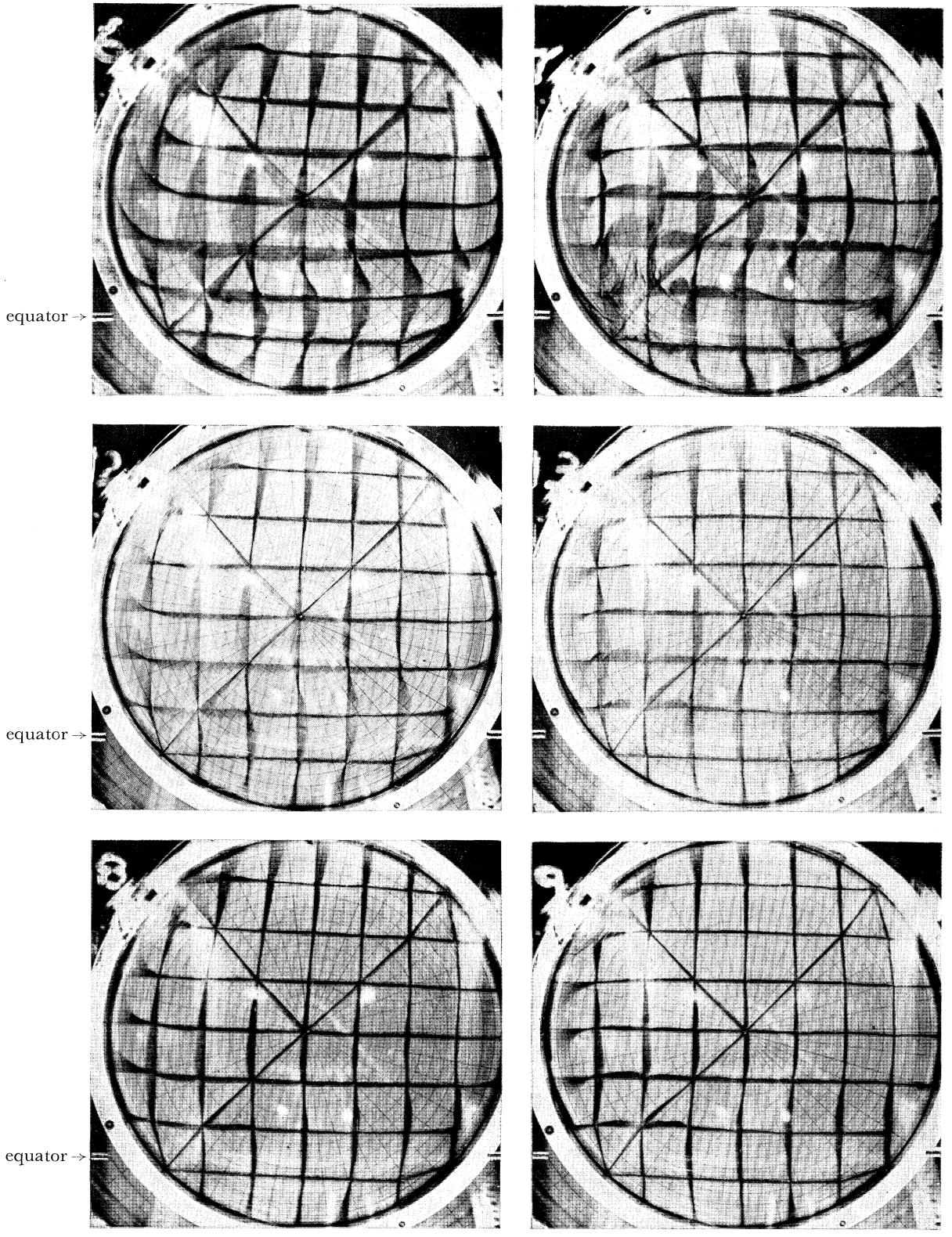

FIGURE 26. Equatorial flow as a function of ω. ($\theta_0 = 13.0°$, $\Omega = 6.32$ rad s^{-1}, $\gamma = 0.00214$ for all pictures.) Positive ω appears on the right, negative ω on the left. (*a*) Lower: $\omega = 0.0297$ rad s^{-1}, $\epsilon_{eq} = 0.00392$, $R_{eq} = 0.111$. Centre: $\omega = 0.0994$ rad s^{-1}, $\epsilon_{eq} = 0.0131$, $R_{eq} = 0.372$. Upper: $\omega = 0.249$ rad s^{-1}, $\epsilon_{eq} = 0.0329$, $R_{eq} = 0.931$.

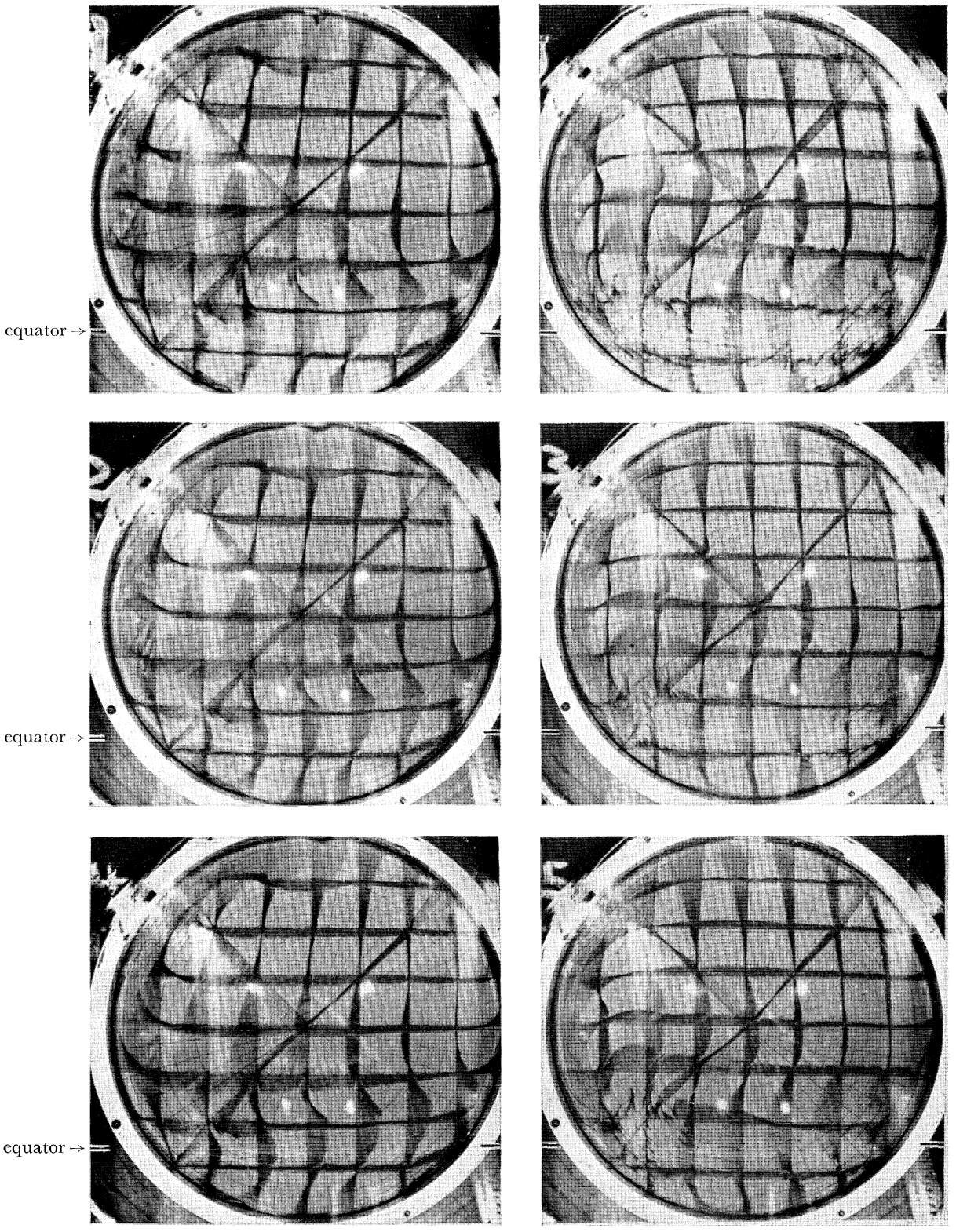

FIGURE 26. (*b*). Lower: $\omega = 0.300$ rad s^{-1}, $\epsilon_{eq} = 0.0396$, $R_{eq} = 1.122$. Centre: $\omega = 0.351$ rad s^{-1}, $\epsilon_{eq} = 0.0463$, $R_{eq} = 1.31$. Upper: $\omega = 0.400$ rad s^{-1}, $\epsilon_{eq} = 0.0528$, $R_{eq} = 1.50$.

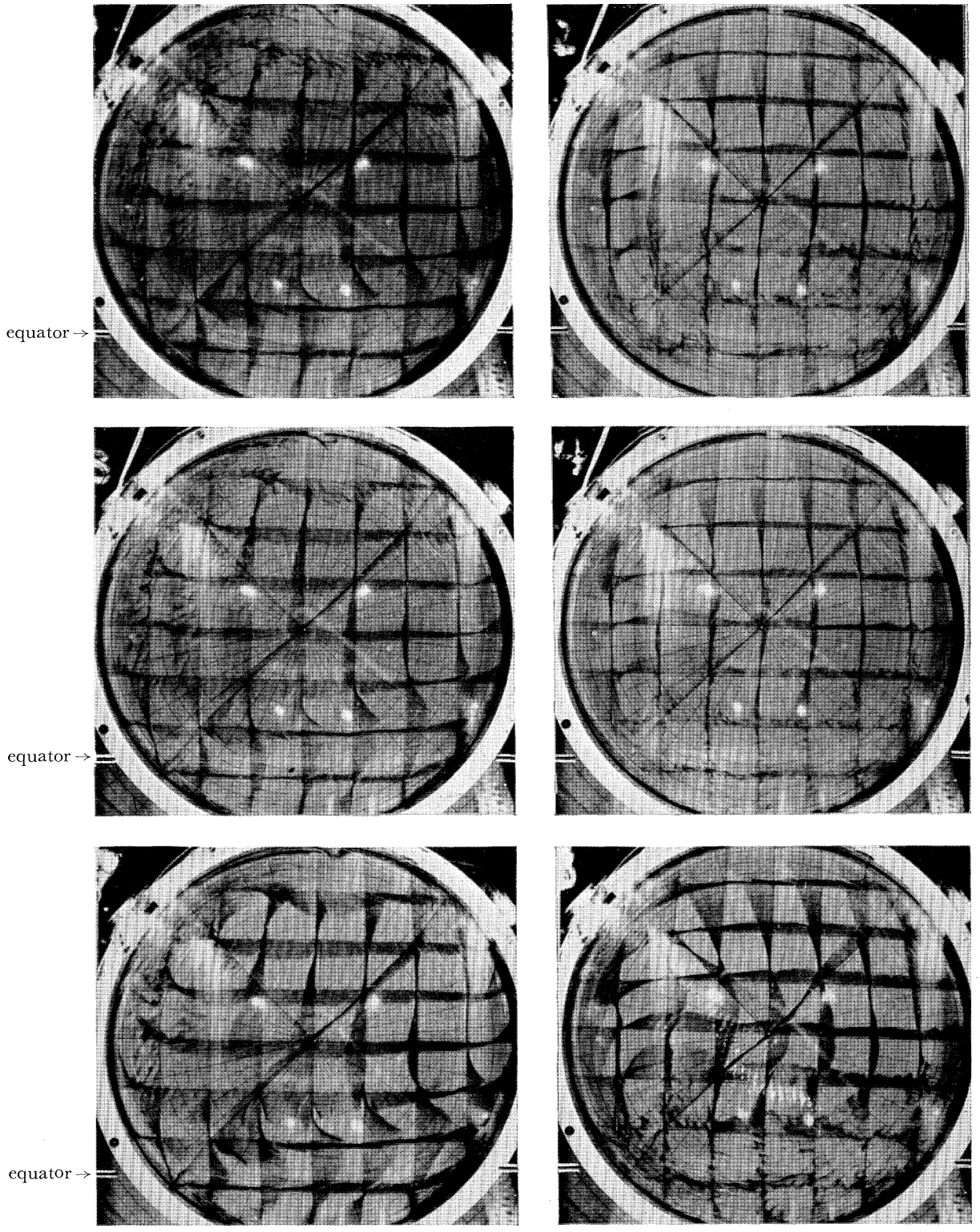

FIGURE 26 (*c*). Lower: $\omega = 0.500$ rad s^{-1}, $\epsilon_{eq} = 0.0660$, $R_{eq} = 1.87$. Centre: $\omega = 0.706$ rad s^{-1}, $\epsilon_{eq} = 0.0932$, $R_{eq} = 2.64$. Upper: $\omega = 0.802$ rad s^{-1}, $\epsilon_{eq} = 0.106$, $R_{eq} = 3.00$.

The equation of continuity in a boundary layer variable is

$$u_x + v_y + \frac{\zeta}{2f} v_\zeta + \left(\frac{f}{2\gamma}\right)^{\frac{1}{2}} w_\zeta = 0.$$

The Ekman layer solutions

$$\left.\begin{aligned} \overset{0}{u}{}^1 &= (\overset{0}{a}{}^1 \sin \zeta_0 + \overset{0}{b}{}^1 \cos \zeta_0)\, e^{-\zeta_0}, \\ \overset{0}{v}{}^1 &= (-\overset{0}{b}{}^1 \sin \zeta_0 + \overset{0}{a}{}^1 \cos \zeta_0)\, e^{-\zeta_0}, \end{aligned}\right\} \tag{5.6}$$

where $$a^0 = V_B - v^G, \quad a^1 = -v^G, \quad b^0 = U_B - u^G, \quad b^1 = -u^G$$

allow explicit integration of (5.6) across the Ekman layers. The resultant two equations govern the interior horizontal function. Elimination of W yields the equation to be satisfied by the interior pressure

$$-(p_{xx} + p_{yy}) + \frac{3}{2(y+c)}(p_x + p_y) - \frac{p_x}{[2\gamma(y+c)]^{\frac{1}{2}}} = \tfrac{1}{4}\sigma(x - 3y - 4c). \tag{5.7}$$

The right-hand side of equation (5.7) is $0(1)$, and exhibits the effect of surface driving on the geostrophic flow. Since the development of the solution is in the nature of a singular perturbation expansion, at this point equation (5.7) must be consistently expanded in γ. Thus p is $0(\gamma^{\frac{1}{2}})$ and a geostrophic Sverdrup relation is immediately evident, namely

$$p_x = (y+c)\, v^G = \frac{\sigma\gamma^{\frac{1}{2}}}{2\sqrt{2}} (y+c)^{\frac{1}{2}} (3y + 4c - x). \tag{5.8}$$

The associated w^G satisfies the inviscid boundary condition at the top surface to accuracy $0(\gamma^{\frac{1}{2}})$. The top Ekman layer is $\gamma^{\frac{1}{2}}$ weaker than the bottom layer; thus, the total Sverdrup transport is to a first approximation, compounded from the meridional geostrophic flow plus the Ekman transport at the driven boundary (Robinson 1965, § 11). The zonal geostrophic flow obtains after integration of (5.8) and evaluation of the resultant free function of y, which depends upon analysis of the side wall boundary layers.

5.2. *Side wall boundary layers of a square basin*

Four dynamically distinct types of side wall boundary layers must be considered for the range of parameters of the linear régime of our experiment. A complicating factor in the circular basin analysis is the continuous change of the boundary layer dynamics with the angle ϕ (figure 3). It is instructive to first consider a similar problem in a square ocean basin, where the transitional dynamics occur in corner regions which need not be considered in detail. Figure 13 shows schematically the distribution of the layers in the plane $z = \frac{1}{2}$, the numerals designating particular types of dynamics.

All of the layers considered have a (horizontal) width thicker than a (vertical) Ekman layer thickness. Thus the description of the vertical dependence of the side wall boundary layers may be considerably simplified by considering regions II to V to have (possibly) important associated Ekman layers at both top and bottom. The Roman numerals thus refer to flows which are interior regions with respect to these vertically directed boundary layers, but which are boundary layers with respect to horizontally directed scaled variables.

The thicknesses of regions II and III are respectively $0(\gamma^{\frac{1}{2}})$ and $0(\gamma^{\frac{1}{4}})$. The flow is entirely geostrophic and hydrostatic and interacts strongly with its Ekman layers, both top and bottom.

Thus these regions may be referred to physically as (top and) bottom frictional boundary layers. Mass conservation involves all three terms in the continuity equation. These boundary layers are in fact contained in the pressure equation (5.7) derived above, evoking respectively the terms p_{xx} and p_{yy} to balance the term $\propto p_x$. The $\gamma^{\frac{1}{2}}$ layer can exist only near a western coast. The approximate equations are solved subject to the boundary conditions $(2f)^{\frac{1}{2}}w \mp v_\xi = 0$, where $\xi = \gamma^{-\frac{1}{2}}x$ at the edges of the Ekman layers ($z = 0, 1$). The explicit solutions are given by

$$u = \gamma^{\frac{1}{2}}\left[\left(\frac{3}{\sqrt{(2f)}} + \frac{\xi}{2f}\right)\chi(y) + \sqrt{(2f)}\,\chi'(y)\right] e^{-\xi/\sqrt{(2f)}} \tag{5.9a}$$

$$v = \chi\, e^{-\xi/\sqrt{(2f)}} \tag{5.9b}$$

$$w = \frac{v}{f}(z - \tfrac{1}{2}) \tag{5.9c}$$

where $\chi(y)$ is an arbitrary function of its argument. The $\gamma^{\frac{1}{4}}$-layer can exist near either a northern or a southern boundary, with the local thickness modified by the local value of $f^{-\frac{1}{4}}$. The variation of f across the narrow current is, however, essential to the dynamics in such a manner that these layers may be appropriately referred to as quasigeostrophic (meteorological vernacular).

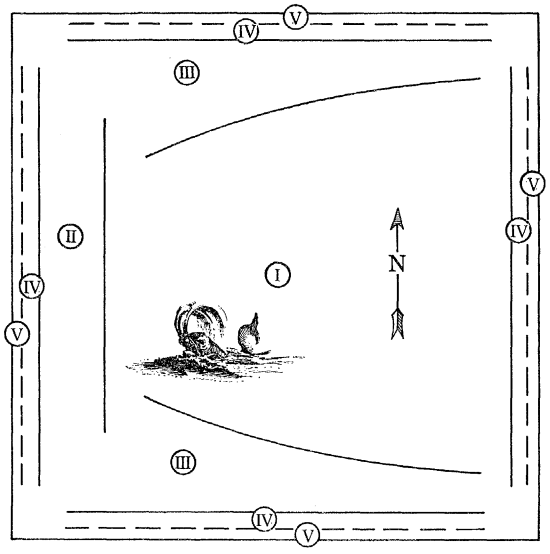

FIGURE 13. Boundary layers in a square basin. The roman numerals designate regions of different dynamics. See text.

The width of regions of type IV is $O(\gamma^{\frac{1}{4}}\lambda)$. The motion is approximately hydrostatic and the relatively strong downstream velocity component is related geostrophically to the cross-stream pressure gradient. However, lateral stress divergence dominates the downstream pressure gradient. Strong interaction again occurs with top and bottom Ekman layers; thus these regions are mixed side and bottom frictional layers. Mass conservation is maintained approximately between the cross-stream and vertical fluxes. For example, if $\eta = \gamma^{\frac{1}{4}}\lambda^{-1}x$ near the western coast, the approximate downstream equation is $\gamma^{\frac{1}{2}}v_{\eta\eta} - fu = 0$, the continuity equation is $u_\eta + w_z = 0$, and the boundary condition at the edges of the Ekman layers ($z = 0, 1$) are $(2f)^{\frac{1}{2}}\lambda w \pm \gamma^{\frac{1}{4}}v_\eta = 0$. The velocity components are found to be

$$u = \left(\frac{2\gamma}{f}\right)^{\frac{1}{2}} v, \tag{5.10a}$$

$$v = \Phi(y)\, e^{-(2f)^{\frac{1}{2}}\eta}, \tag{5.10b}$$

$$w = \frac{2(\frac{1}{2}-z)}{\lambda(2\gamma f)^{\frac{1}{4}}} v, \tag{5.10c}$$

where $\Phi(y)$ is an arbitrary function. The solutions near an east coast are, except for sign changes, the same as (5.10). The $\gamma^{\frac{1}{4}}\lambda$-layers near a northern or southern coast are modified by effects due to the parameter A, since the relatively strong longitudinal flow component augments the Coriolis acceleration due to the horizontal component of rotation.

The regions of type V are of width $0(\gamma^{\frac{1}{3}}\lambda)$. Mass continuity is maintained two dimensionally as in the $\gamma^{\frac{1}{4}}\lambda$-layers. Lateral stresses enter in both the downstream and vertical momentum equations, and horizontal Coriolis terms are important.

Consider the role of the various boundary layers in the satisfaction of the no-slip boundary conditions on the side walls of the square ocean basin vertically interior to the Ekman layers of the side wall boundary layers. Suppose the circulation to be driven by an $0(1)$ distribution of bottom velocity (top velocity 0). Then the bottom Ekman layer velocities are $0(1)$, with an associated mass transport $0(\gamma^{\frac{1}{2}})$, as is the mass transport of the $0(\gamma^{\frac{1}{2}})$ (Sverdrup) geostrophic velocities of region I. The $0(\gamma)$ transport of the upper Ekman layer is negligible. The $\gamma^{\frac{1}{2}}$ mass flux in the driven bottom Ekman layer flows under the side wall boundary layers into a narrow corner region ($\sim (\nu/2\Omega \sin\theta_0)^{\frac{1}{2}}$ cm on a side) and emerges into region V as an $0(\gamma^{\frac{1}{2}})$ flow normal to the side wall. This flow has locally the identical normal transport of the incoming Ekman flow because of the two-dimensional character of mass conservation in region V. Thus this flow adds together with the normal component of flow from region I to satisfy the normal velocity component side wall condition. Near the eastern wall the contributions from I and V are the only leading contributions to the normal flow component, but near the northern and southern wall the contributions from region III aid in the satisfaction of the normal flow condition, as do the contributions from regions II and IV near the western wall.

The discussion given here depends upon a knowledge of the relative amplitude in γ, λ of the velocity components in the various layers. Since the circulations of the layers broader than type V which contribute to the satisfaction of the normal flow condition themselves close in type V regions through their associated (top and bottom) Ekman layers and corners (see equations 5.9, 10), the normal transport of these associated Ekman layers must be properly taken into account.

All around the square the type IV boundary layers serve to contribute to the satisfaction of the no-slip condition on the tangential horizontal velocity component. The leading contributions to the tangential component near the western, northern and southern, and eastern boundaries are, respectively, $0(1, \gamma^{\frac{1}{4}}, \gamma^{\frac{1}{2}})$. Thus the strongest boundary current is the $0(1)$ western boundary 'Gulf Stream'. The no-slip condition on the vertical velocity is accomplished in region V.

In consideration of the normal flow condition it is useful to note that (see equation 5.10a, c) the approximate two-dimensional character of the mass conservation of the $\gamma^{\frac{1}{4}}\lambda$-layers (IV) implies that the normal mass influx into these regions all effluxes through associated Ekman layers. Thus IV, its associated Ekman layers and corners, and its associated V exhibit a recirculating double celled structure. The other layers (II, III) involved to leading order in the normal flow condition are completely geostrophic and hydrostatic and are therefore necessarily contained in the full pressure equation (5.7). The above considerations imply a simple boundary condition on the total geostrophic velocity component (I, II, III) near the side walls, namely,

that its transport be equal and opposite to that of all the associated Ekman layers (top and bottom) including, of course, the forced Ekman bottom transport from the interior.

The physical length scales corresponding to the non-dimensional eastern and western coastal layer thicknesses are

$$\text{(II)} \quad f^{\frac{1}{2}}\gamma^{\frac{1}{2}}L = \left(\frac{\nu}{2\Omega \sin\theta_0}\right)^{\frac{1}{2}} \frac{R_0}{H} \tan\theta_0,$$

$$\text{(IV)} \quad \gamma^{\frac{1}{4}}\lambda f^{-\frac{1}{4}}L = \left(\frac{\nu H^2}{2\Omega \sin\theta_0}\right)^{\frac{1}{4}},$$

$$\text{(V)} \quad \gamma^{\frac{1}{3}}\lambda f^{-\frac{1}{3}}L = \left(\frac{\nu H}{2\Omega \sin\theta_0}\right)^{\frac{1}{3}}.$$

The condition for the existence of the boundary layer structure as discussed above is found to be $\lambda < \gamma^{\frac{1}{4}}$. For $\lambda > \gamma^{\frac{1}{4}}$ type II and IV layers are replaced by regions in which the downstream momentum balance involves both lateral stress and pressure gradient as well as Coriolis acceleration. The Ekman layers are weak and side friction is dominant. These layers are of thickness $\gamma^{\frac{1}{3}}\lambda^{\frac{2}{3}}L = (\nu R_0/2\Omega\cos\theta_0)^{\frac{1}{3}}$. Thus bottom friction dominates side friction in a thin system if $H < (\nu/2\Omega\sin\theta_0)^{\frac{1}{6}}(R_0\tan\theta_0)^{\frac{2}{3}}$.

5.3. *Approximate results for a circular basin*

For the parameter range of the linear régime of our experiment $\lambda < \gamma^{\frac{1}{4}}$ and bottom frictional layers exist. Thus the full pressure equation (5.7) plays a central role. The detailed analysis for the circular basin is being performed by a numerical integration of equation (5.7) in polar coordinates, subject to the transport boundary condition on the total geostrophic flow

$$\left\{\left(\frac{2\gamma}{f}\right)^{\frac{1}{2}} \frac{p_r}{f} + \left[1 - \left(\frac{2\gamma}{f}\right)^{\frac{1}{2}}\right] \frac{p_\phi}{f} = \left(\frac{\gamma}{2f}\right)^{\frac{1}{2}} \sigma. \right. \tag{5.11}$$

Equation (5.11) results simply from adding the radial component of the top and bottom Ekman layer transports (solutions 5.6) to the geostrophic transport and evaluating the result at $r = 1$.

Although the results of the numerical analysis are not yet available, it is possible to carry over some of the analytical results for the square basin to the circle for purposes of comparison with experiment. An approximate expression for the zonal interior geostrophic flow may be obtained through use of a transport boundary condition which may be expected to be valid in the range $|y| < \sim\frac{1}{2}$. Corresponding to the east coast condition in the square, the geostrophic transport is simply matched to the forced Ekman transport for $x > 0$. There results

$$\left(\frac{\gamma}{2\sin\phi}\right)^{\frac{1}{2}} [(U_B + V_B)\cos\phi + (V_B - U_B)\sin\phi] - \frac{1}{\sin\phi} = 0. \tag{5.12}$$

Upon integration of (5.8) the pressure is given by

$$p = \frac{\sigma\gamma^{\frac{1}{2}}}{2\sqrt{2}} [f^{\frac{1}{2}}(-\tfrac{1}{2}x^2 + 3yx + 4cx) + \Pi(y)]. \tag{5.13}$$

The geostrophic zonal velocity is thus

$$u^G = \frac{-1}{f} \frac{\sigma\gamma^{\frac{1}{2}}}{2\sqrt{2}} [\tfrac{1}{2}f^{-\frac{1}{2}}(-\tfrac{1}{2}x^2 + 3yx + 4cx) + f^{\frac{1}{2}}3x + \Pi'(y)], \tag{5.14}$$

Equation (5.12), together with equation (5.13) evaluated at $x = +\sqrt{(1-y^2)}$ allows the evaluation of $\Pi'(y)$;

$$\Pi'(y) = \frac{2f^{\frac{1}{2}}}{\sqrt{(1-y^2)}} + \frac{yf^{\frac{1}{2}}}{\sqrt{(1-y^2)}}\left(-\sqrt{(1-y^2)} + 3y + 4c\right)$$
$$- 3f^{\frac{1}{2}}\sqrt{(1-y^2)} - \frac{1}{2f^{\frac{1}{2}}}\left(\frac{1-y^2}{2} + 3y\sqrt{(1-y^2)} + 4c\sqrt{(1-y^2)}\right), \tag{5.15}$$

and thus u^G is determined.

The east and west coast boundary layer analysis should be applicable to the circular basin sufficiently close to $\phi = 0, \pi$. The expression (5.9b) for the velocity parallel to the boundary in the $\gamma^{\frac{1}{2}}$-layer (II) in cylindrical coordinates becomes

$$v = \chi(\phi)\exp\left[\frac{\cos\phi}{\sqrt{(2f\gamma)}}(1-r)\right]. \tag{5.16}$$

Although further analysis is necessary to determine the arbitrary function $\chi(\phi)$ for all ϕ, it is possible to evaluate $\chi(\pi)$ by noting that the total meridional transport integrated across the plane $y = 0\,(-1 \leqslant x \leqslant 1,\ 0 \leqslant z \leqslant 1)$ must vanish.

The leading contributions ($0(\gamma^{\frac{1}{2}})$) come from the boundary current (5.16), the (Sverdrup) geostrophic drift, and the bottom Ekman layer, but the latter transport vanishes upon integration in x. The contribution to the transport from the flow of type IV (5.10b) is $0(\gamma^{\frac{1}{4}}\lambda)$, which provides a correction to the western boundary current of about 15 %. The final dimensional expression

$$v = \frac{2\omega L}{1-\lambda(2f)^{-\frac{3}{4}}\gamma^{-\frac{1}{4}}}\left[\exp-\left(\frac{1+x}{\sqrt{(2f\gamma)}}\right) - \exp-\left[(1+x)\frac{(2f)^{\frac{1}{4}}}{\lambda\gamma^{\frac{1}{4}}}\right]\right], \tag{5.17}$$

results for the tangential velocity in the western boundary current.

6. Comparison of theory and experiment

Formulae for the structure of the flow in the linear régime have been presented in § 5; in this section the results of experiment are compared with the predictions of the theory. Good agreement between theory and experiment is indicated, thus establishing the validity of the β-plane analysis as applied to the experimental system in this parameter range.

6.1. *The meridional flow*

The meridional velocity was measured as a function of ω, γ, and of position. Figure 14 is a plot of the measured v against ω at a representative point for fixed main rotation rate. The least squares fit to the points is

$$v = (1.70 \pm 0.06)\,\omega\ (\mathrm{cm\,s^{-1}}),$$

the uncertainties arising from the sources discussed in § 3.3. The linear theory (5.8) predicts a straight line whose equation is

$$v = 1.78\omega\ (\mathrm{cm\,s^{-1}}).$$

Although the nonlinear parameter ϵ ranges from 0.00244 to 0.205, no systematic deviation from a linear relation between v and ω is indicated. The agreement exhibited indicates that a geostrophic Sverdrup relation is indeed valid for this system.

The γ-dependence of the meridional flow is presented in figure 15. Although considerable scatter is exhibited, a least squares fit to the points yields

$$v \propto \gamma^{+(0.40\pm0.06)},$$

which is consistent with the theoretical exponent 0.5. The scatter in the points is due to the small range of speeds accessible.

The slow variation of the meridional velocity upon position is exhibited in figure 16. The theoretical displacements are compared directly with the observed displacements traced from a representative photograph in the linear régime. In the interior the agreement is good; the discrepancies occur in the north and south. As indicated in § 5.3, corrections to the leading order in the γ-expansion are not expected to be negligible in those regions.

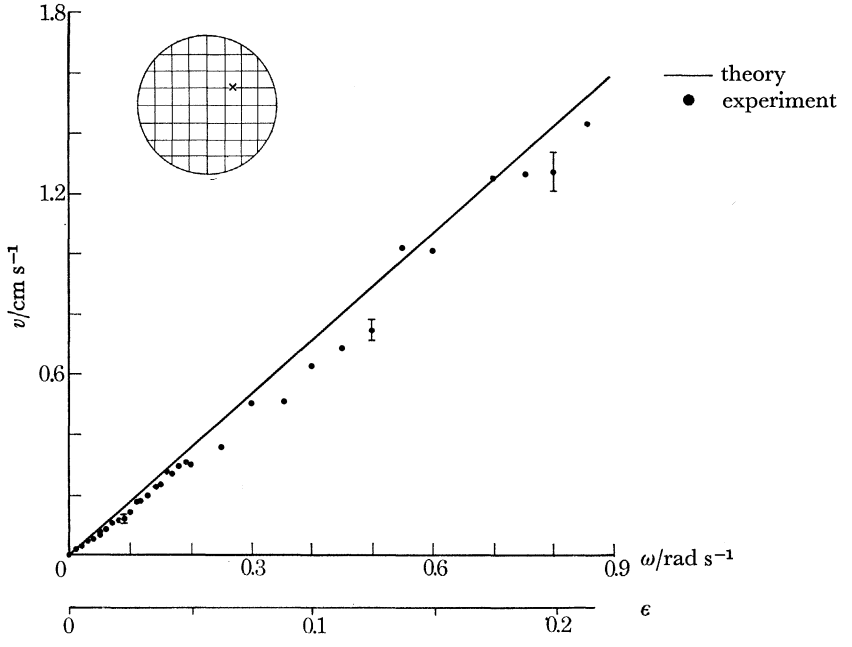

FIGURE 14. Interior meridional 'Sverdrup' flow v as a function of ω and ϵ. ($\theta_0 = 31.5°$, $\Omega = 6.32$ rad s^{-1}, $\gamma = 0.00245$.) The data was taken at the point indicated by the cross in the circle at upper right, $x = 7.62$ cm, $y = 5.08$ cm. The error bars denote typical uncertainties.

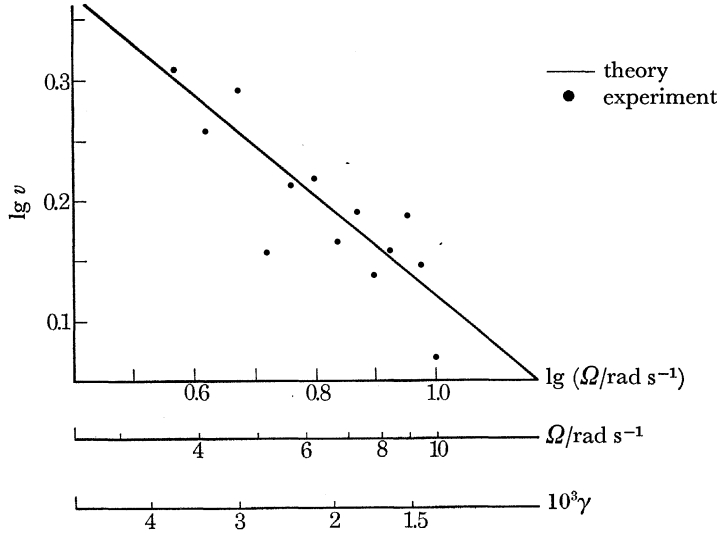

FIGURE 15. Ω and γ dependence of interior meridional flow. The line has the theoretically predicted slope of $\frac{1}{2}$. Data taken at $x = 7.62$ cm, $y = 5.08$ cm. ($\omega = 0.0970$ rad s^{-1}, $\theta_0 = 13.0°$.)

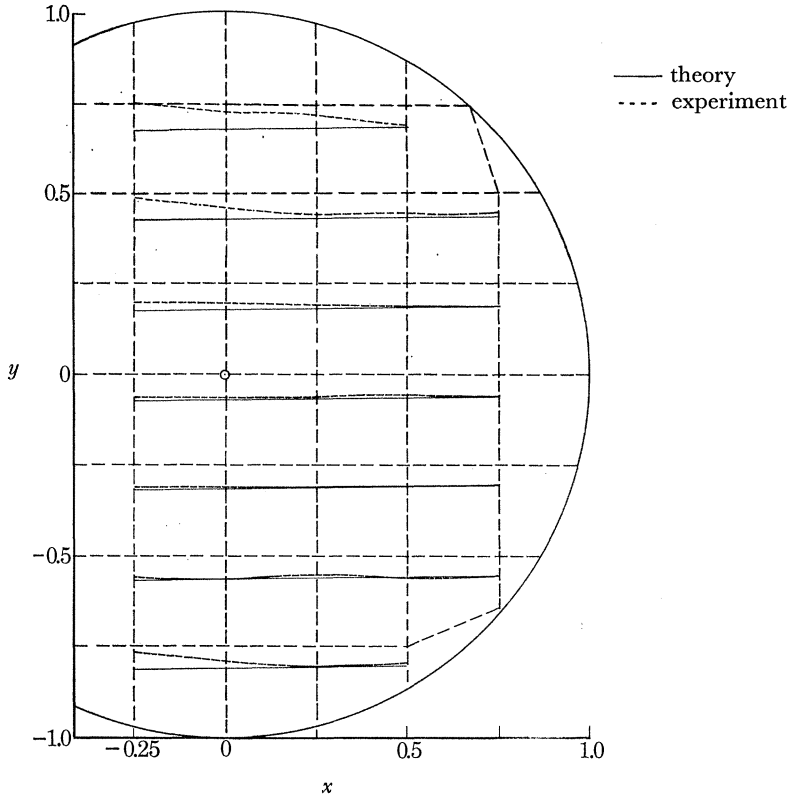

FIGURE 16. Comparison of predicted and observed meridional displacements from a single photograph. (Measuring grid indicated by dashed lines.) ($\theta_0 = 31.4°$, $\Omega = 6.31$ rad s^{-1}, $\omega = 0.00872$ rad s^{-1}, $\epsilon = 0.00218$, $\gamma = 0.00245$, $\gamma^{\frac{1}{2}} = 0.0495$.)

6.2. *The zonal flow*

The zonal flow was also measured as a function of ω, γ, and of position. Figure 17 is a plot of the measured u against ω at a representative point for fixed main rotation rate. The least squares fit to the points is

$$u = (0.764 \pm 0.020)\omega \,(\text{cm s}^{-1}).$$

The theory (5.14) predicts a straight line whose equation is

$$u = 0.803\omega \,(\text{cm s}^{-1}).$$

The γ dependence of the measured zonal flow is

$$u \propto \gamma^{+(0.55 \pm 0.03)},$$

which is consistent with the theoretical exponent 0.5 (figure 18). Although fewer data were taken than for figure 15, the scatter is less; this is probably fortuitous.

The variation of the zonal velocity upon position is exhibited in figure 19. The agreement in u is comparable to that in v; the zonal flow is sensitive to the distribution of $\Pi'(y)$ (5.14) and thus credibility is lent to the boundary layer analysis.

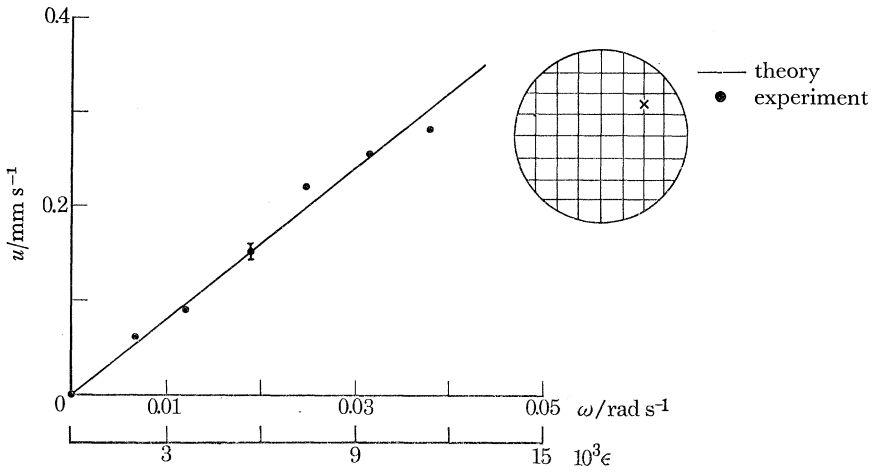

FIGURE 17. Interior zonal flow as a function of ω and ϵ. The data were taken at the point indicated by the cross in the circle at upper right, $x = 10.16$ cm, $y = 7.02$ cm. Error bars denote typical uncertainties. ($\theta_0 = 28.9°$, $\Omega = 5.03$ rad s^{-1}, $\gamma = 0.00299$.)

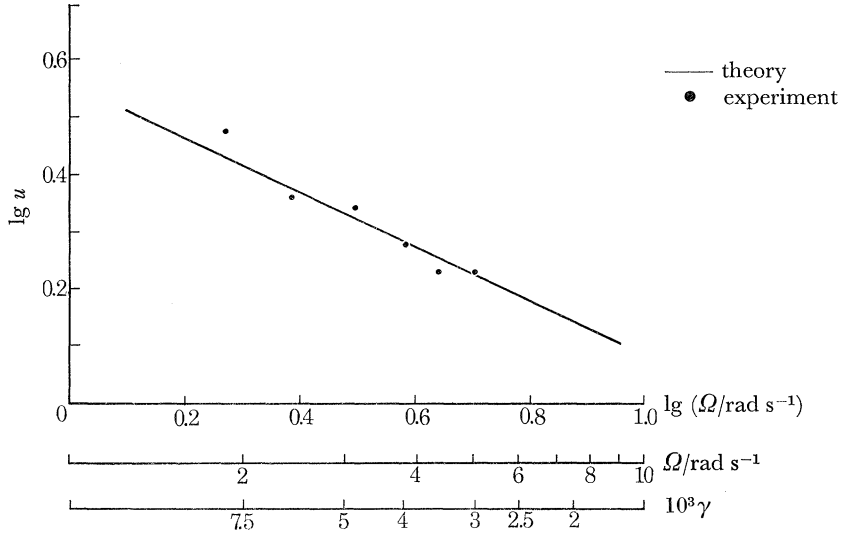

FIGURE 18. Ω and γ dependence of interior zonal flow. ($\omega = 0.0120$ rad s^{-1}, $\theta_0 = 28.9°$.) The straight line has the theoretically predicted slope of $\frac{1}{2}$. Data taken at $x = 5.58$ cm, $y = 7.62$ cm.

6.3. *The western boundary current*

Here the e-folding width of the current as a function of γ, the magnitude of the velocity at a given point as a function of ω, and a single experimental velocity profile are compared with theory.

The γ-dependence of the e-folding width is determined from a plot of the logarithm of the slopes of several curves of $\lg v_\phi$ against $(1-r)$, each curve obtained for a single value of γ. Nineteen such curves were obtained from photographs of the boundary current, and the e-folding width for each curve was determined by the method of least squares. The logarithms of the resulting widths were then plotted against the logarithm of Ω in order to exhibit the γ-dependence (figure 20). A slope of 0.552 ± 0.054 results; the errors have been computed by standard techniques. The theory predicts a slope of 0.5. The good agreement establishes the existence of the $O(\gamma^{\frac{1}{2}})$ boundary layer in this experiment.

A determination of the azimuthal velocity at the point $\phi = \pi$ and $x = 17.8\,\mathrm{cm}$ as a function of ω for fixed $\gamma = 0.0025$ is presented in figure 21. The least squares fit to all the points yields $v = (9.41 \pm 0.30)\omega\,(\mathrm{cm\,s^{-1}})$. Theory predicts (5.17), $v = 8.53\omega\,(\mathrm{cm\,s^{-1}})$. The deviation from the

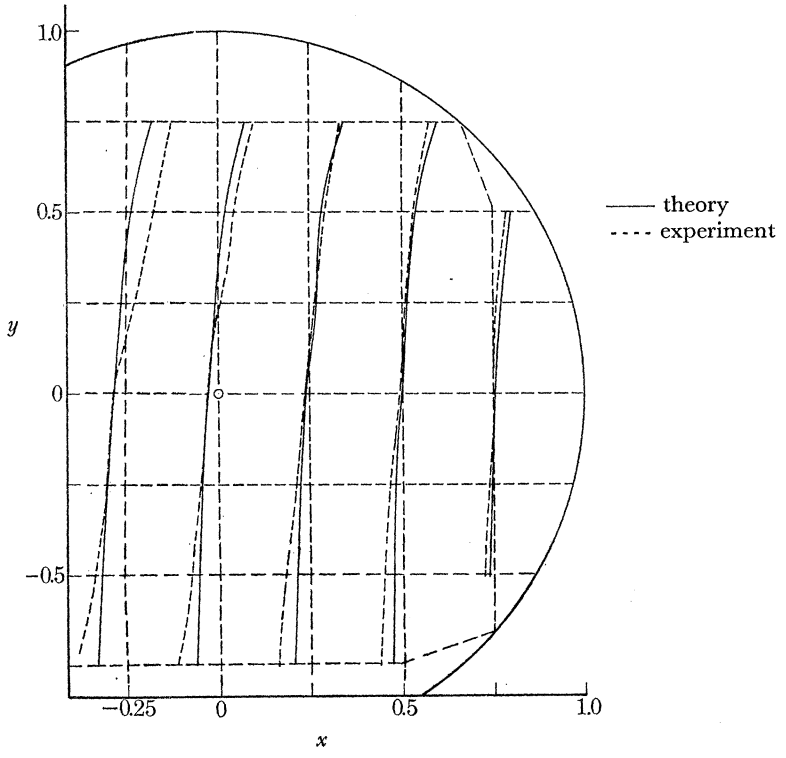

FIGURE 19. Comparison of predicted and observed zonal displacements from a single photograph. ($\theta_0 = 31.4°$, $\Omega = 6.31\ \mathrm{rad\,s^{-1}}$, $\omega = 0.00872\ \mathrm{rad\,s^{-1}}$, $\epsilon = 0.00218$, $\gamma = 0.00245$, $\gamma^{\frac{1}{2}} = 0.0495$.)

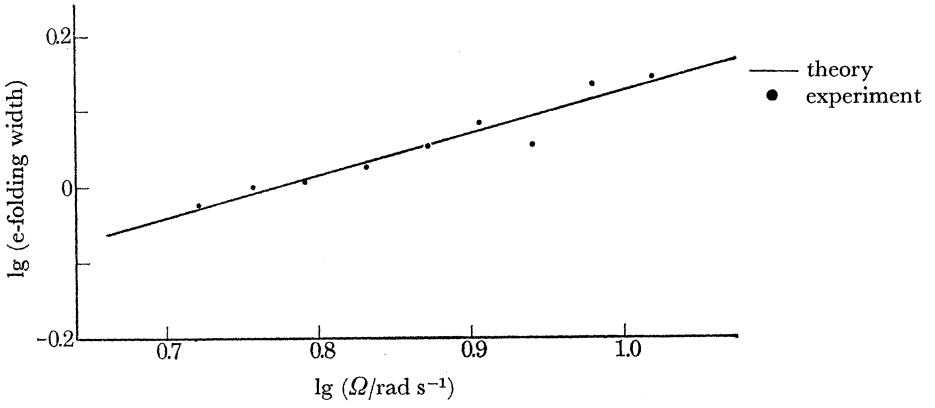

FIGURE 20. E-folding width of western boundary current as a function of Ω along the line $y = 0$. Linear theory predicts a slope of $\frac{1}{2}$; a least squares fit to the experimental points yields a slope of 0.552 ± 0.054. ($\theta_0 = 31.4°$, $\omega = 0.0159\ \mathrm{rad\,s^{-1}}$, ϵ: 0.00405 – 0.00234, γ: 0.00292 – 0.00147.)

theoretical line appears systematic. The linear theory holds strictly in the limit $\epsilon \to 0$ and nonlinear effects are expected to appear in this boundary layer when $\epsilon > 0(\gamma^{\frac{1}{2}})$. (For this data $\gamma^{\frac{1}{2}} = 0.05$.) If a least squares fit be made (somewhat arbitrarily) for the points $\epsilon < 0.024$, $v = (8.38 \pm 0.25)\omega$ results, in good agreement with theory.

A velocity profile (for the same γ) well within the linear régime ($\epsilon = 0.0039$) is presented in figure 22. This is a reduction from a single photograph, and although the lack of averaging increases the uncertainties, agreement is satisfactory with the profile of equation (5.17).

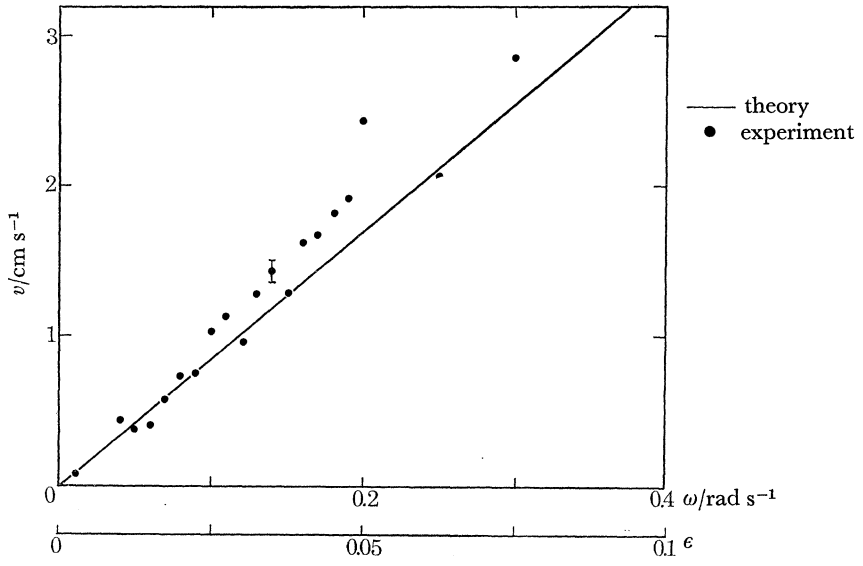

FIGURE 21. Interior western boundary current northward flow as a function of ω and ϵ at $\phi = \pi$ and $x = 17.8$cm. Error bars denote typical uncertainties. ($\theta_0 = 31.4°$, $\Omega = 6.31$ rad s^{-1}, $\gamma = 0.00245$, $\gamma^{\frac{1}{2}} = 0.0495$.)

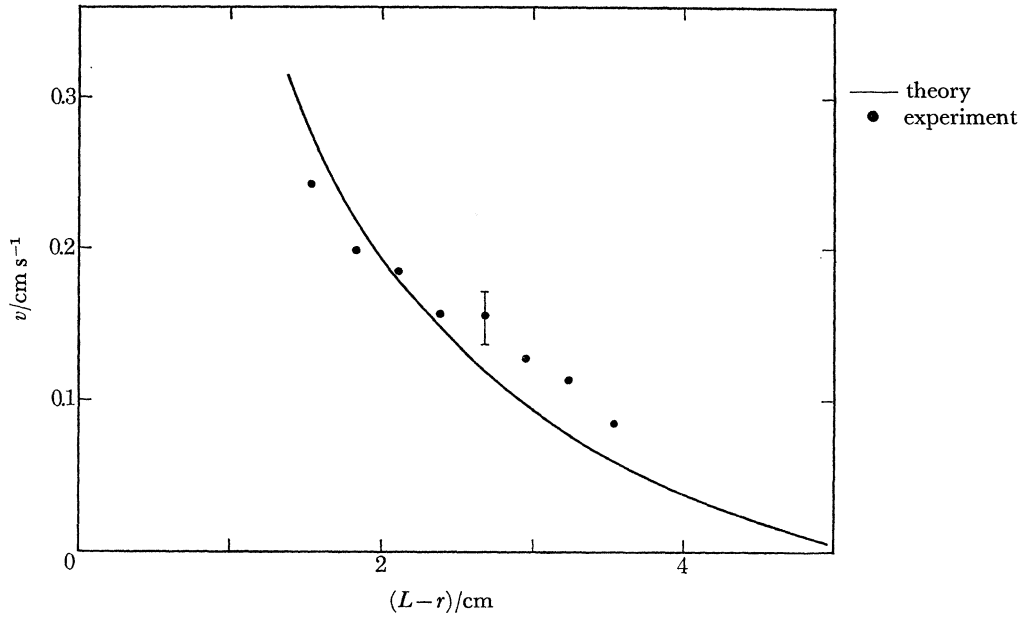

FIGURE 22. Velocity profile of western boundary current at $\phi = \pi$. Error bars denote typical uncertainties. ($\theta_0 = 31.4°$, $\Omega = 6.21$ rad s^{-1}, $\epsilon = 0.00390$, $\gamma = 0.00249$, $\gamma^{\frac{1}{2}} = 0.0499$.)

6.4. *The eastern boundary current*

At the eastern boundary, the interior meridional flow is brought to zero, theoretically in a weak boundary layer $0(\lambda\gamma^{\frac{1}{4}})$ in thickness. The e-folding width of the boundary flow has been determined experimentally as a function of ω along the line $y = 0$. Curves of velocity against

position were obtained from single photographs, and the e-folding widths, determined by least squares methods, are plotted in figure 23. An average of the points for $\epsilon < 0.024$ yields an e-folding width of 1.55 ± 0.20 mm; the theory predicts 1.87 mm.

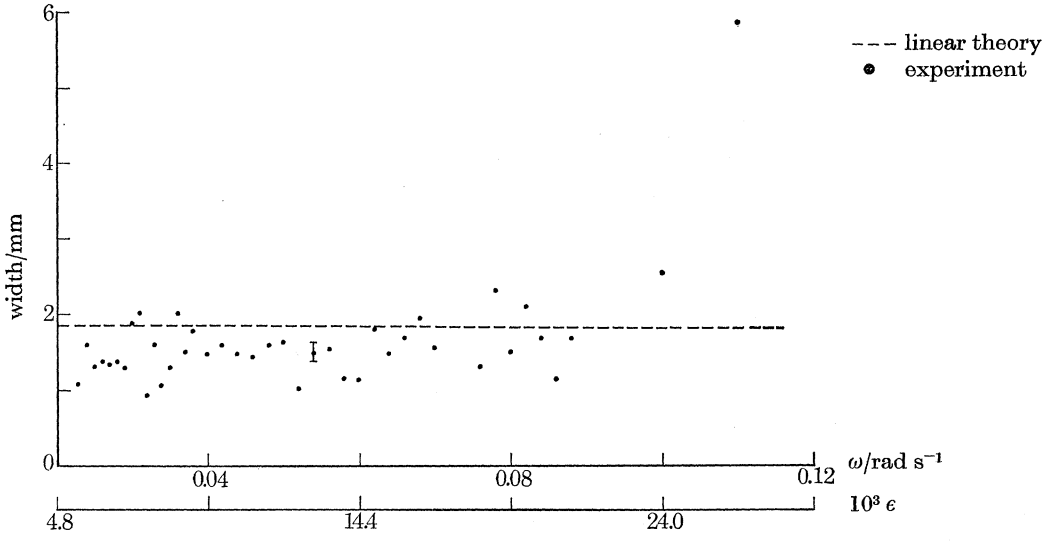

FIGURE 23. Measured e-folding width of eastern boundary current against ω and ϵ along $y = 0$ compared to prediction of linear theory. ($\theta_0 = 31.4°$, $\Omega = 6.31$ rad s^{-1}, $\gamma = 0.00245$, $\gamma^{\frac{1}{2}} = 0.0495$.) Note large displacement of final point. Error bars denote typical uncertainties.

7. PHENOMENOLOGY

The remainder of the experimental results to be presented here cannot as yet be subject to the same critical comparison with theory as those of the last sections. As both the theory and experiment of the nonlinear subtropical gyre are in progress, the results presented are preliminary. The equatorial experimental results are exploratory but quantitative; the theory has been initiated.

7.1. *The nonlinear subtropical gyre*

For relatively large values of ω, ϵ increases and the circulation changes qualitatively (figure 11). Recall that the interior geostrophic velocity (figure 14) remains linear in ω and thus exhibits no nonlinear effect. Since the strong western boundary current develops speeds 0 (10 cm s^{-1}), and the chemical technique is limited to speeds less than ~ 3 cm s^{-1}, quantitative data is not yet available for large ϵ. Techniques for the measurement of rapid velocities in our apparatus are under investigation.

However, it is possible with the present technique to make a quantitative measurement in the nonlinear régime. The point in the fluid where u and v are simultaneously zero will be referred to as the 'centre of the gyre'. Because of the spacing of the wire grid, a study of flow photographs could locate this feature of the flow only within a circle of radius 1 cm. Figure 24 illustrates the position of this point as a function of ω and ϵ. The scatter in angle simply reflects the coarseness of measurement. As ϵ increases beyond 0.05, the centre of the gyre moves rapidly towards the north and west.

For large enough ϵ the circulation appears to be not entirely steady. The sequential photographs of figure 11 indicate the changing nature of the flow in time as delineated by a steady

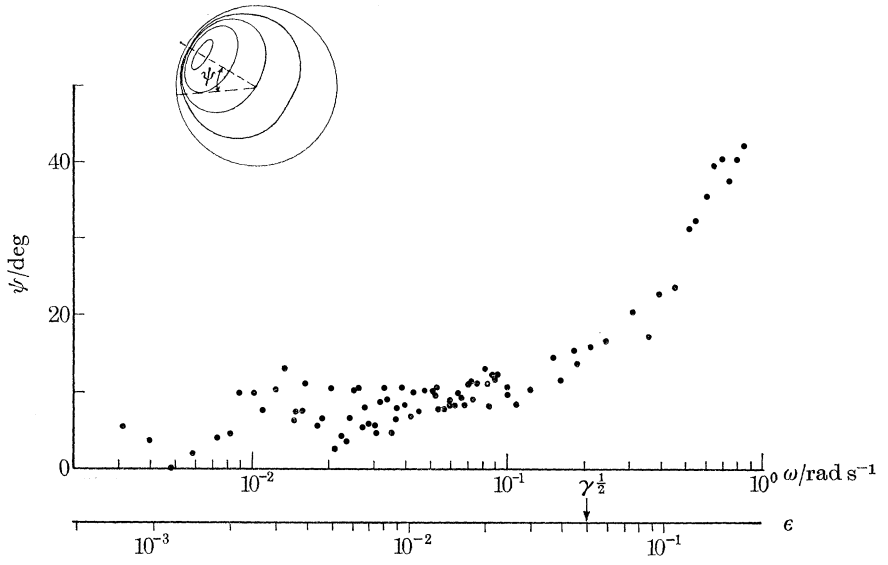

FIGURE 24. Position of centre of gyre as a function of ϵ and ω.
($\theta_0 = 31.4°$, $\Omega = 6.31$ rad s^{-1}, $\gamma = 0.00245$, $\gamma^{\frac{1}{2}} = 0.0495$.)

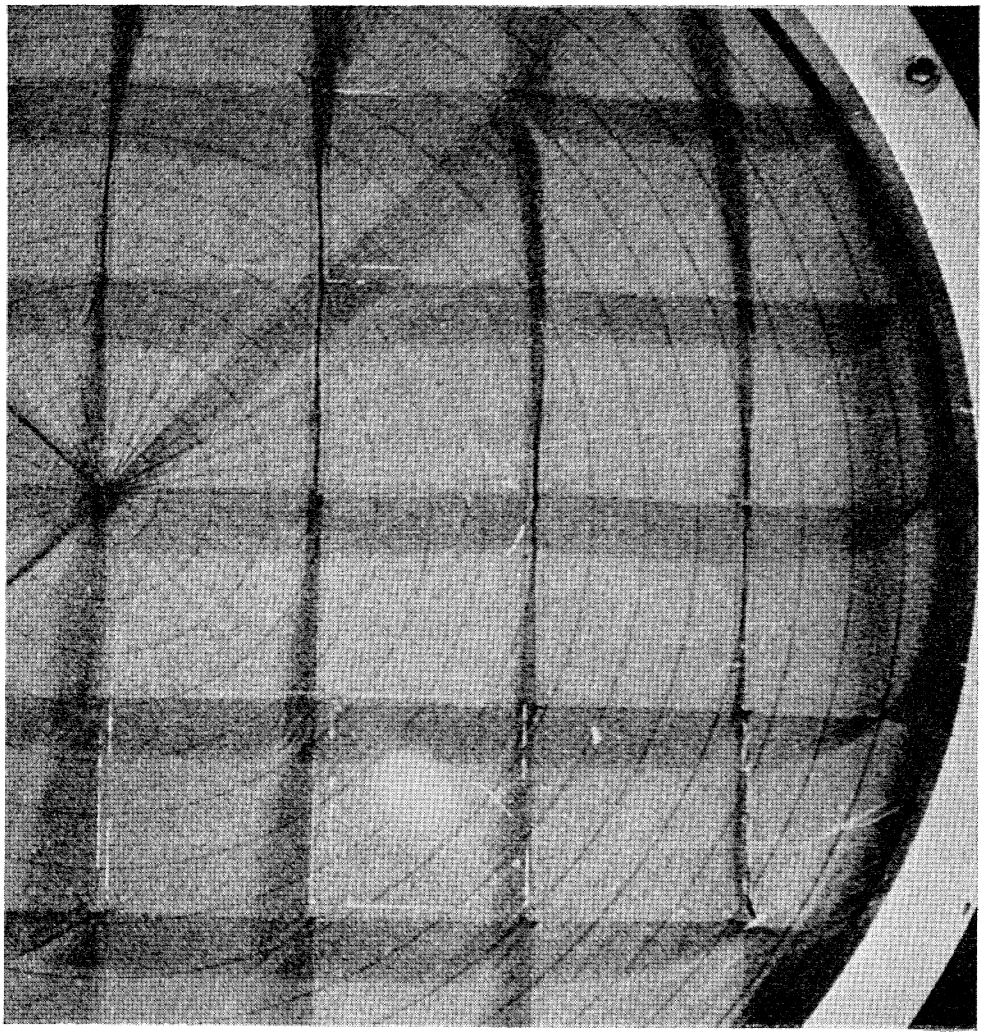

FIGURE 25. Photograph of a northward eastern boundary current (at right centre).
($\theta_0 = 31.4°$, $\epsilon = 0.0260$, $\gamma = 0.00245$, $\gamma^{\frac{1}{2}} = 0.0495$.)

release of coloured fluid. Motion pictures of this phenomenon reveal a possible periodic motion superimposed on the strong circulation, an obvious oscillation of the oval in the second quadrant. The dye lines located between the centre of the gyre and the centre of the basin approached each other and receded in about 7 s. The shortest period normal mode (Rossby wave) for the basin has been calculated to be 7.4 s. Further more careful experimentation is necessary to establish the nature of the observed time dependence.

A nonlinear effect is also observable in the eastern boundary current. For $\epsilon > 0.024$, the width rapidly increases (figure 23). Although only a single point appears on the figure for large ϵ, its reliability is established by crude width determinations from many photographs at high ϵ; the rapid width change is clearly evident. The increasing width is, in fact, associated with a northward flowing current (see figure 25). Although poleward eastern boundary currents have been observed in the ocean (Wooster & Reid 1963), their dynamics and role in the general circulation is not sufficiently well understood to permit comparison with the laboratory experiment at this time.

To estimate the onset of nonlinear behaviour, effective local Rossby numbers for various regions of the flow have been calculated, based upon the scales and amplitudes appropriate to the linear régime square basin. Region I to IV (figure 13) and their associated Ekman layers have been considered.

Nonlinear effects are negligible in the broad western boundary current (II) and also in its Ekman layer when $\epsilon\gamma^{-\frac{1}{2}} \ll 1$. Thus nonlinearity becomes important in these regions when $\epsilon \sim \gamma^{\frac{1}{2}}$. The same criterion pertains to the quasigeostrophic current (III), but in its Ekman layer the weaker condition $\epsilon \sim \gamma^{\frac{1}{4}}$ holds. The smallest value of the external Rossby number for incipient nonlinearity is $\epsilon \sim \gamma^{\frac{1}{4}}\lambda$, which condition pertains simultaneously in all the layers of width $0(\gamma^{\frac{1}{4}}\lambda)$ (IV) and all their associated Ekman layers.

These criteria are useful in the interpretation of figures 23 and 24. For those measurements $\gamma = 0.00245$, $\gamma^{\frac{1}{2}} = 0.0495$, $\gamma^{\frac{1}{4}}\lambda = 0.0110$. The rapid broadening of the eastern boundary current and the start of the migration of the centre of the gyre are seen to occur for $\epsilon \sim 0.020$, halfway between these two criteria.

7.2. *The equatorial undercurrent*

When the latitude of the centre of the basin is less than 16°, a zonal current is observed in the vicinity of the equators of the defining spheres, flowing in the direction opposite to the longitudinal component of the surface forcing velocity (figure 10). The axis of this equatorial undercurrent lies on the equators in the west but deviates northward to the east. This deviation may be due to the distribution of driving velocity, or to the circular boundary, or perhaps may have a more profound dynamical or kinematical origin.

A series of studies were carried out at $\theta_0 = 13.0°$ (where the equators of the defining spheres pass midway between the centre of the basin and the most southerly point of the rim) in order to determine the dependence of the structure of the flow on the parameters. This θ_0 is the best compromise to achieve a strong zonal component of surface velocity and yet have the equator isolated from the southern boundary. Flow patterns as a function of ω are presented in figure 26, plates 14 to 16. The equatorial flow is observed to join smoothly to the extra-equatorial flow in the following way: the *eastward* equatorial undercurrent (forced by a clockwise surface velocity) is fed from the north and south by the interior geostrophic drift, a region of divergence at the western side of the basin feeds both the eastward equatorial current and the northward western boundary current; whereas the *westward* flowing equatorial undercurrent (forced by a counter-

clockwise surface velocity) loses water to the north and south interior geostrophic drift, and flows towards a convergence with the southward flowing western boundary current.

The equatorial current system is apparently 'symmetrical' with respect to the sign of ω for small $|\omega|$. The behaviour as $|\omega|$ increases depends on the intensification of the equatorial flow together with the tendency of the western boundary current to intensify, with the maximum of the speed moving northwards ($\omega < 0$) or southwards ($\omega > 0$) (recall figure 24). When $\omega \sim 0.25$ rad s^{-1} (figure 26*c*) a streakiness has fully developed in the dye pattern in the west equatorial convergence zone, probably due to high speed but possibly an incipient instability. As ω increases the east equatorial flow develops an irregularity which appears to migrate westward. For $\omega > 0.5$ rad s^{-1} westward equatorial undercurrent is no longer observable, and even a qualitative description of the flow is inaccessible to the chemical technique. In contrast the eastward flowing undercurrent ($\omega < 0$) remains well defined and measurable for even the highest $|\omega|$ studied.

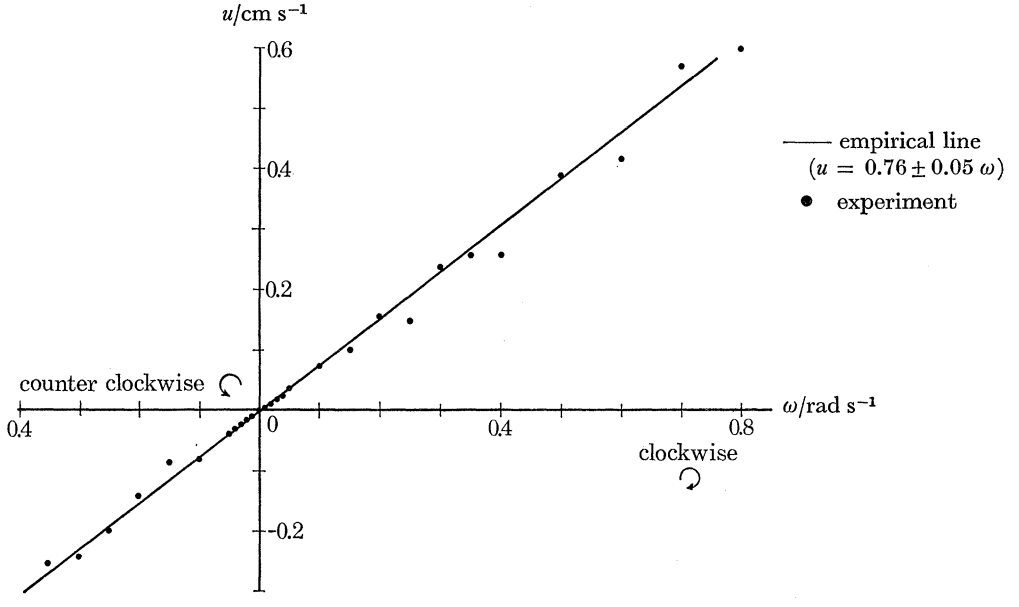

FIGURE 27. Maximum zonal velocity of equatorial undercurrent as a function of ω at $x = 0$. ($\theta_0 = 13.0°$, $\Omega = 6.32$ rad s^{-1}, $\gamma = 0.00214$.)

Four quantitative studies were carried out on the undercurrent: the width and speed as a function of ω and Ω at $x = 0$ ($\phi = -\frac{1}{2}\pi$). A least squares fit for the speeds (figure 27) yields the equation $u = (0.76 \pm 0.10)\omega$ (cm s^{-1}). The width of the current (defined as the distance between the zeros of u) is a slowly varying function of ω (figure 28). Note the apparent stronger Ω–dependence of the westward flowing current, probably associated with the increasing strength of the incoming western boundary current. The speed is a slowly varying function of Ω (figure 29); the least squares fit from a logarithmic plot yields $\Omega^{+(0.84\pm0.08)}$. The empirical width dependence on Ω (figure 30) is $\Omega^{+(0.17\pm0.05)}$.

The measurements of maximum speed (u_{eq}) and the width ($\mathscr{L}$) allow an estimate to be made of the relative importance of terms in the momentum equations at mid-depth in the equatorial region. We assume that all terms contribute to the continuity equations, that $\partial/\partial x$, $\partial/\partial z$ remain $0(1)$ but $\partial/\partial y \sim 0\,(\mathscr{L}^{-1})$, and that horizontal pressure gradients are of the same order as Coriolis terms across the region. Then the leading terms are those characteristic of the geostrophic mid-latitude flow with the addition of Coriolis accelerations resulting from the locally horizontal

component of basic rotation (the local effective Λ is $\Lambda\mathscr{L}^{-2} \sim 0(1)$). The most significant departure from this balance occurs in the longitudinal equations. The relevant local Rossby number is $\epsilon_{eq} = \epsilon u_{eq}\mathscr{L}^{-2}$. The vertical frictional term dominates the cross-stream frictional term in the ratio $\mathscr{L}^2\lambda^{-2}$; whence the most important Reynolds number is $R_{eq} = \epsilon u_{eq}\gamma^{-1}$. The

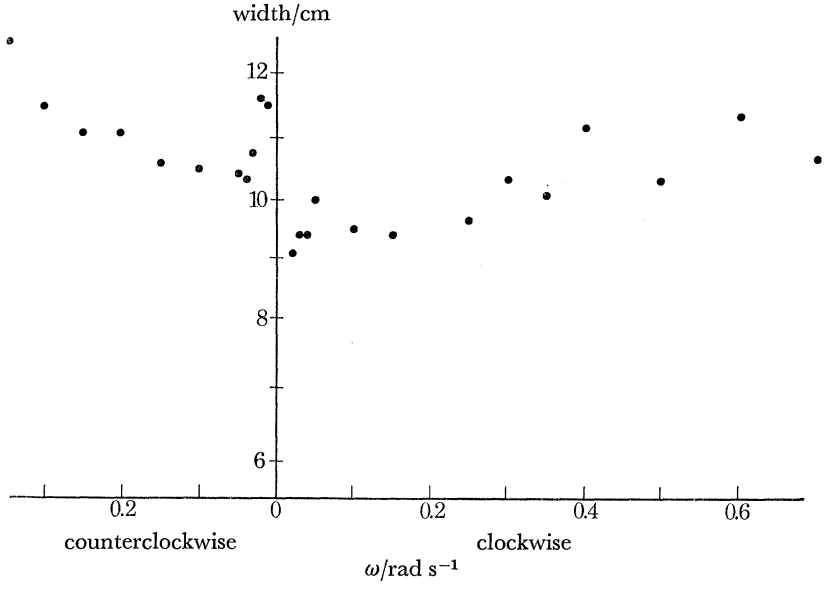

FIGURE 28. Width of equatorial undercurrent (distance between two zeros of zonal velocity) as a function of ω at $x = 0$. ($\theta_0 = 13.0°$, $\Omega = 6.32$ rad s^{-1}, $\gamma = 0.00214$.)

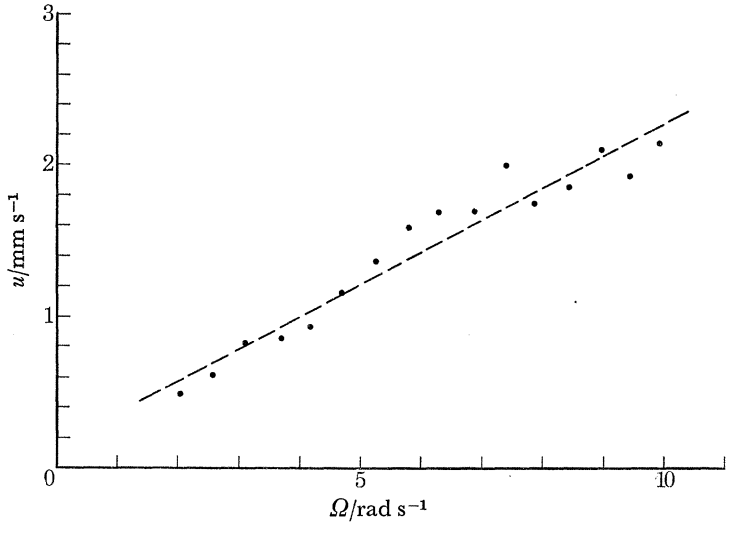

FIGURE 29. Maximum velocity of equatorial undercurrent as a function of Ω at $x = 0$. ($\theta_0 = 13.0°$, $\omega = 0.0969$ rad s^{-1}.) The dotted line represents the least squares power law fit to these points.

empirical results imply $R_{eq} = 5\omega$. In the range of $|\omega|$ investigated (0.01 to 0.8 rad s^{-1}), $10^{-3} < \epsilon_{eq} < 10^{-1}$, $0.04 < R_{eq} < 3$. It is of some interest to note that $Re_{eq} = 1$ when $\omega = 0.27$ and to speculate as to the relevance of this parameter to the phenomenon occurring in the westward undercurrent for $0.25 < \omega < 0.40$ rad s^{-1}. However, the occurrence of horizontal Coriolis

terms means that boundary layer structure in the vertical is possible (although the usual Ekman layers cannot exist equatorially) and a more important Reynolds number may be associated with such a layer.

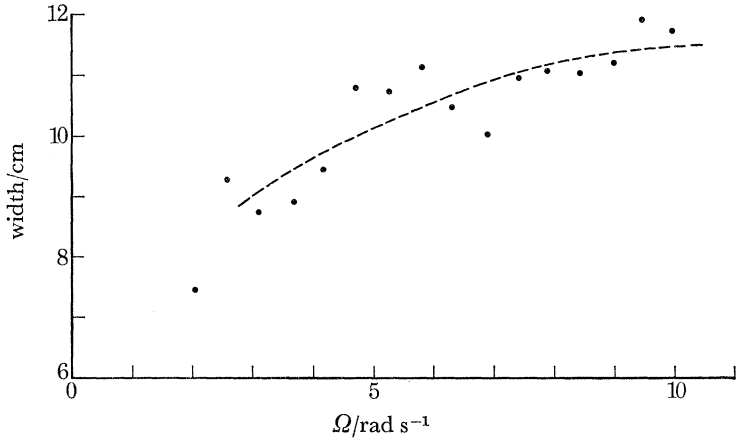

FIGURE 30. Width of equatorial undercurrent as a function of Ω at $x = 0$. ($\theta_0 = 13.0°$, $\omega = 0.0969$ rad s^{-1}.) The dotted line represents the least squares power law fit to these points.

8. CONCLUDING REMARKS

The model constructed has provided a variety of interesting phenomena relevant to the general circulation of a barotropic ocean. Good agreement has been found between the experimental results and the prediction of linear boundary layer analysis for a subtropical gyre on the β-plane. In particular, the Sverdrup vorticity balance and the existence of bottom frictional boundary currents have been verified. Predicted Rossby numbers for the onset of nonlinear behaviour of the gyre have been found in reasonable agreement with observed onset; the position of the centre of the nonlinear gyre has been measured. The equatorial currents have been studied extensively as functions of all the variable parameters and an apparent instability observed.

Study is in progress of details of the various horizontal and vertical boundary layers for comparison with the numerical analysis for the circular basin. The nonlinear study will be extended with the techniques under development for the measurement of large velocities. Further study of the observed time dependence of the flow in the nonlinear régime is intended and a search for resonant modes under time dependent forcing is to be carried out with special apparatus which has already been constructed.

The success of the present experiment points the way toward the design of a variety of other oceanically relevant laboratory experiments through modification of the present equipment or construction of more specialized apparatus. A change of western coastal topography could provide an experimental basis for the study of topographical control of bottom frictional boundary layers and associated separation questions. A thinner ocean (plausible with higher rotation rates) would reduce the importance of the horizontal Coriolis terms so that a more geophysical equatorial model could be achieved. A thin spherical annulus could provide a geometry for the study of atmospherically relevant equatorial dynamics. Special geometry is also of interest for the study of polar flows; e.g. the coupled general circulation of a subpolar gyre and an Antarctic circumpolar current could be investigated.

Notation

The following is a list of symbols employed in the text:

(R, θ, ψ)	spherical coordinates in the radial, latitudinal and longitudinal directions
(w, v, u)	corresponding velocity components relative to a sphere rotating with angular velocity Ω
Ω	magnitude of the rotation of the model
ν	kinematic viscosity
ρ	density
p	deviation of the pressure from its static value
R_0	radius of the inner sphere
H	radial distance between the spherical surfaces
θ_0	latitude of the centre of the spherical circle
L	radius of the spherical circle
(z, y, x)	surface coordinates in the radial, latitudinal and longitudinal directions
(r, ϕ)	surface polar coordinates centred at $(x = 0, y = 0)$
ω	magnitude of rotation of the lower block
τ	a characteristic time scale
δ	$\dfrac{\tau}{2\Omega \cos\theta_0}\left(\dfrac{R_0}{L}\right)$ (a non-dimensional time scale)
γ	$\dfrac{\nu R_0}{2\Omega \cos\theta_0 H^2 L}$ (an Ekman number)
ϵ	$\dfrac{\omega R_0}{2\Omega \cos\theta_0 L}$ (a Rossby number)
λ	H/L (an aspect ratio)
Λ	HR_0/L^2 (a geometrical parameter which measures Coriolis acceleration caused by the locally horizontal component of rotation)
f	$c + y$ (a non-dimensional Coriolis parameter)
c	$(R_0/L)\tan\theta_0$
U_B	longitudinal velocity of the bottom block
V_B	latitudinal velocity of the bottom block
σ	sense of rotation of the bottom block (counterclockwise $+1$, clockwise -1)
$\zeta_{0,1}$	$(f/2\gamma)^{\frac{1}{2}}z$, $(f/2\gamma)^{\frac{1}{2}}(z-1)$ (vertical boundary layer variables)
u^G, v^G, w^G	interior velocity components
$u^{0,1}, v^{0,1}$	boundary layer contributions to velocity
Π, Φ, χ	functions of y only
η	$\gamma^{\frac{1}{4}}\lambda^{-1}x$ (a horizontal boundary layer variable)
ξ	$\gamma^{-\frac{1}{2}}x$ (a horizontal boundary layer variable)
u_{eq}	maximum non-dimensional velocity of equatorial undercurrent
$\mathscr{L}$	non-dimensional width of equatorial undercurrent
ϵ_{eq}	$\epsilon u_{eq}\mathscr{L}^{-2}$ (an equatorial Rossby number)
R_{eq}	$\epsilon u_{eq}\gamma^{-1}$ (an equatorial Reynolds number

The support of the Office of Naval Research which made this experiment possible is acknowledged with gratitude (Grants number NOOO 14-67-A-0298-0011, NR 083–201 to Harvard University). It is a pleasure to thank Miss Patricia Jaskun for her help in calculations and to acknowledge the technical assistance of Mr Georges Weatherly.

REFERENCES

Baker, D. J. 1966 A technique for the precise measurement of small fluid velocities. *J. Fluid Mech.* **26**, 573–575.

Baker, D. J. 1967 Shear layers in a rotating fluid. *J. Fluid Mech.* **29**, 165–175.

Faller, A. J. 1963 An experimental study of the instability of the laminar Ekman boundary layer. *J. Fluid Mech.* **15**, 560–576.

Fultz, D. 1965 Private communication.

Greenspan, H. P. 1968 *The theory of rotating fluids*, chapter 5. Cambridge University Press.

Lamb, H. 1932 *Hydrodynamics*, §343. Cambridge University Press.

Munk, W. H. 1950 On the wind-driven ocean circulation. *J. Met.* **7**, 79–93.

Robinson, A. R. 1965 Oceanography: in *Research frontiers in fluid dynamics* (ed. by R. J. Seeger and G. Temple), pp. 504–533. New York: Interscience.

Robinson, A. R. 1970 Boundary layers in ocean models. To appear in *Annual Review of Fluid Mechanics*. Vol. II (Ed. W. R. Sears). Palo Alto: Annual Reviews, Inc.

Stommel, H. 1965 *The Gulf Stream*. Berkeley: University of California Press.

Sverdrup, H. U., Johnson, M. W. & Fleming, R. H. 1942 *The oceans—their physics, chemistry and general biology*. Englewood Cliffs, New Jersey: Prentice-Hall.

Tatro, P. R. & Mollo-Christensen, E. L. 1967 Experiments on Ekman layer instability. *J. Fluid Mech.* **28**, 531–543.

Webster, T. F. 1965 Measurement of eddy fluxes of momentum in the surface layer of the Gulf Stream. *Tellus* **17**, 239–245.

Wooster, W. S. & Reid, J. A., Jun. 1963 Eastern boundary currents: in *The sea: ideas and observations on progress in the study of the seas* **2**, 253–280. New York: Interscience.

Wyrtki, K. 1964 Total integrated mass transports and actual circulation in the eastern South Pacific Ocean: in *The atmosphere and sea in motion* (ed. by B. Bolin). pp. 47–52. New York: Rockefeller Institute Press.

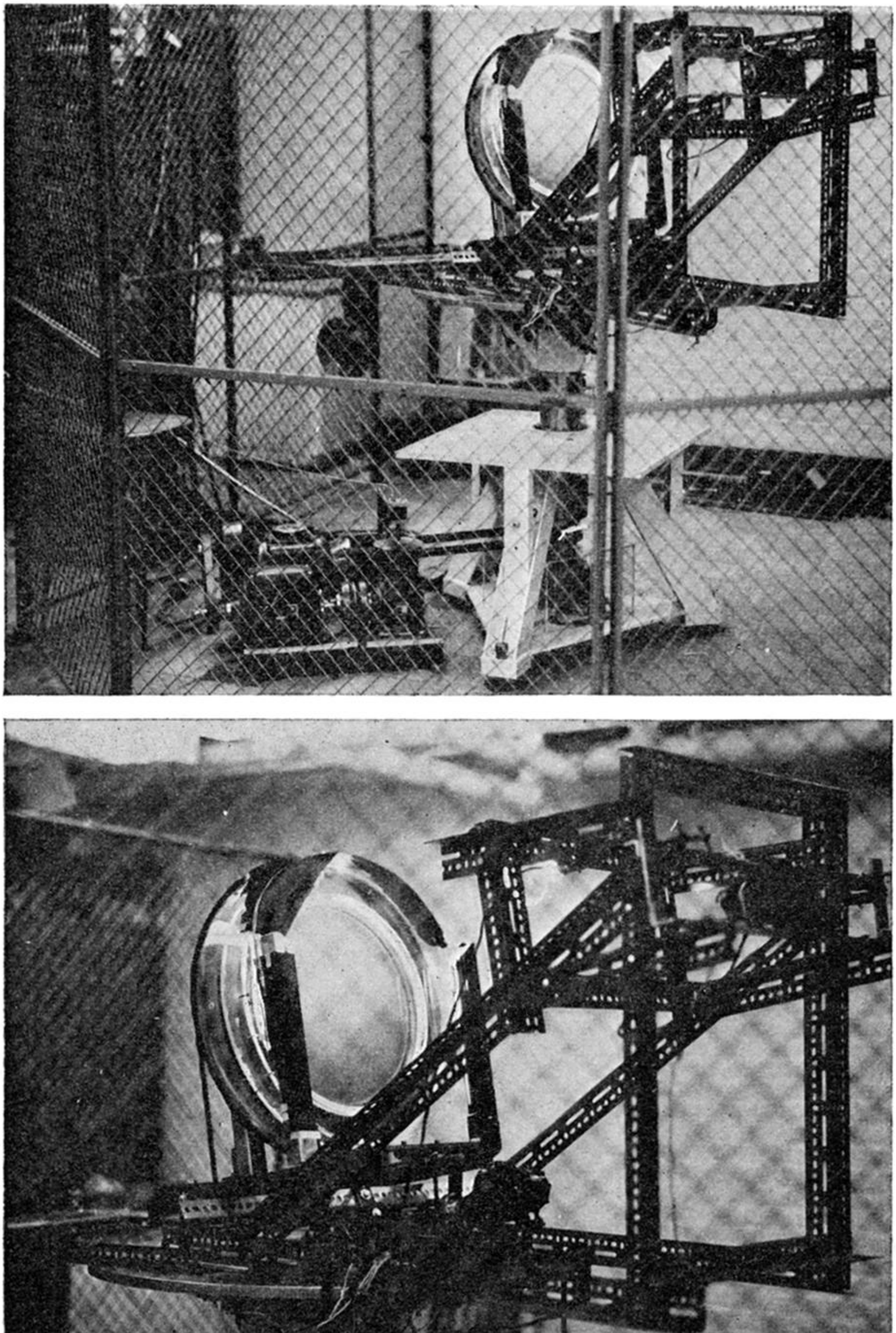

FIGURE 6. Above: the experimental apparatus, rotating table and drive mechanism. Below: the apparatus, relative drive mechanism (lower centre) and motorized camera (upper right).

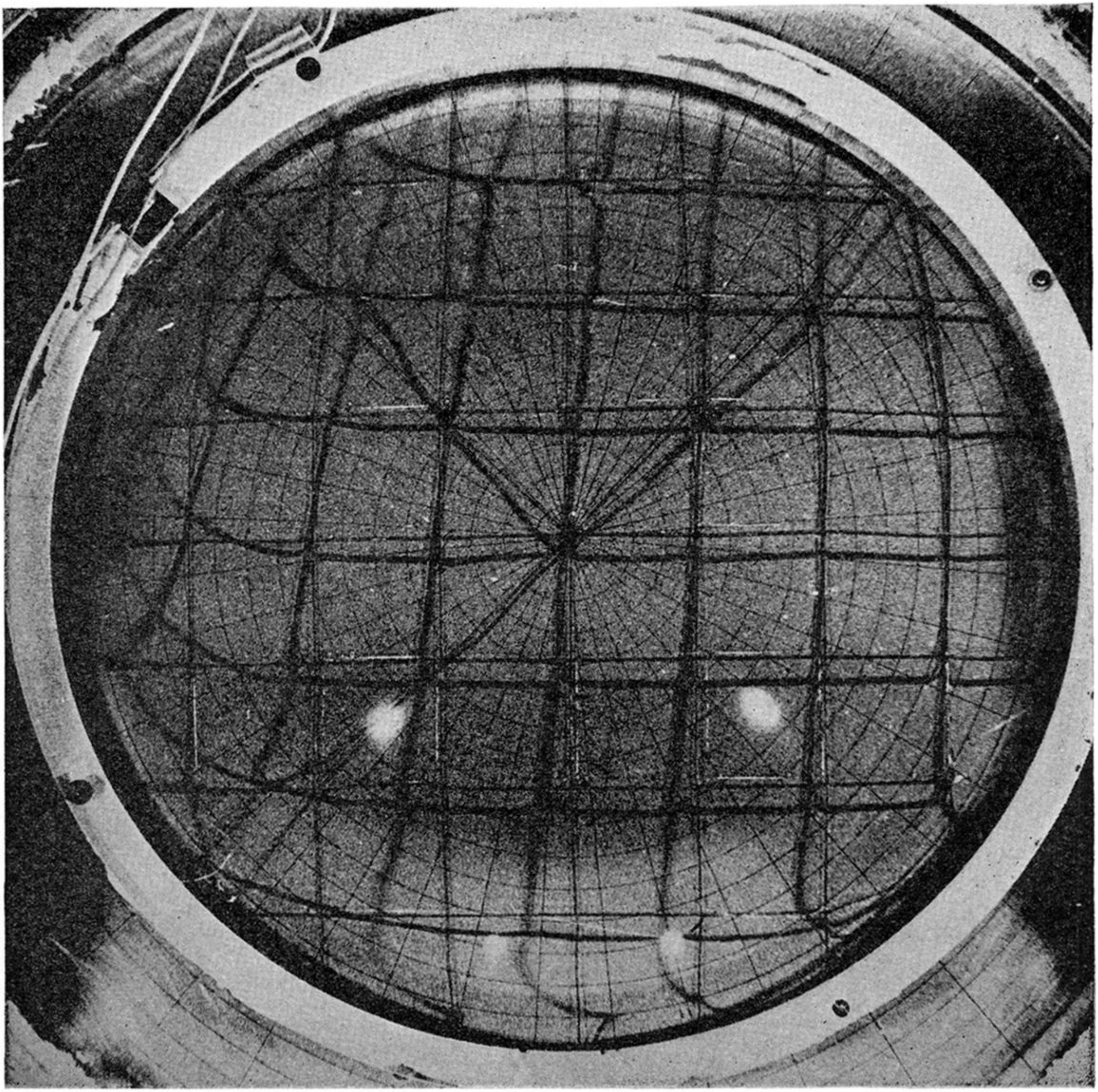

FIGURE 9. Position of ink lines 24 s after current pulse, illustrating general features of extra-equatorial flow. ($\theta_0 = 31.4°$, $\Omega = 6.31$ rad s^{-1}, $\omega = 0.0270$ rad s^{-1}, $\epsilon = 0.00661$, $\gamma = 0.00245$, $\gamma^{\frac{1}{2}} = 0.0495$.)

$\epsilon = 0.089$
$\gamma = 0.0063$
$\gamma^{\frac{1}{2}} = 0.079$
$\omega = 0.142\ \text{rad s}^{-1}$

equator →

$\Omega = 2.10\ \text{rad s}^{-1}$

$\theta_o = 0°$

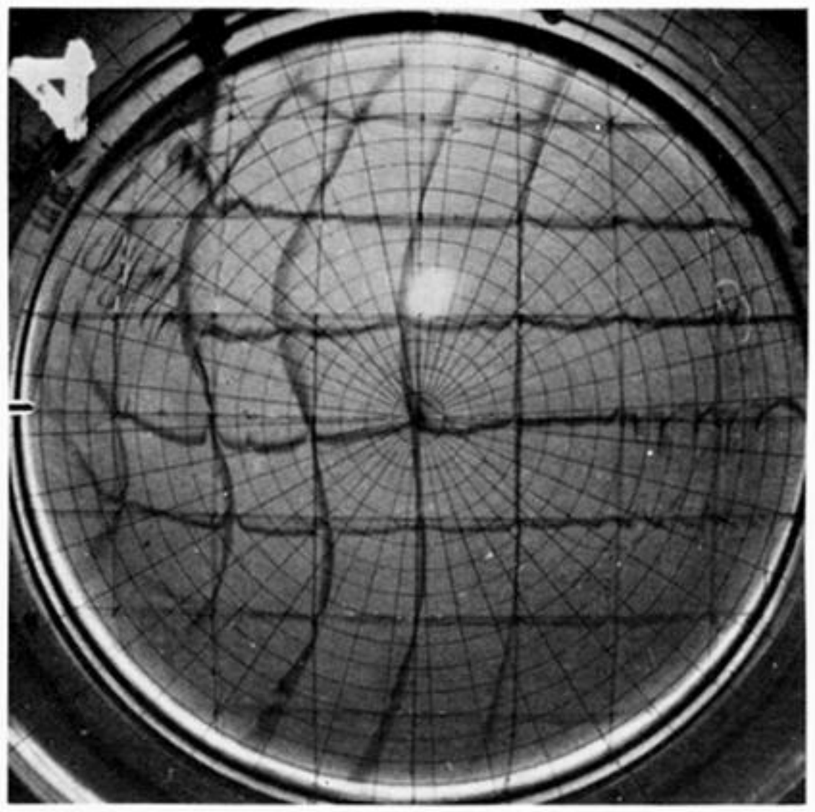

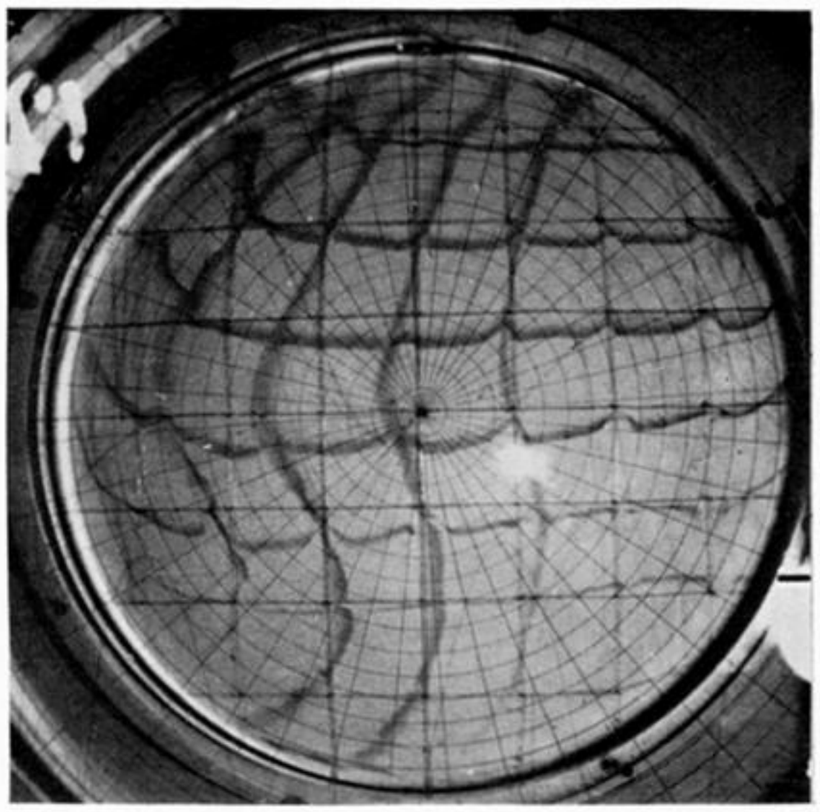

$\epsilon = 0.091$
$\gamma = 0.0063$
$\gamma^{\frac{1}{2}} = 0.079$
$\omega = 0.145\ \text{rad s}^{-1}$
$\Omega = 2.10\ \text{rad s}^{-1}$

← equator

$\theta_o = 6.7°$

$\epsilon = 0.038$
$\gamma = 0.0065$
$\gamma^{\frac{1}{2}} = 0.081$
$\omega = 0.059\ \text{rad s}^{-1}$
$\Omega = 2.10\ \text{rad s}^{-1}$

$\theta_o = 16°$

equator →

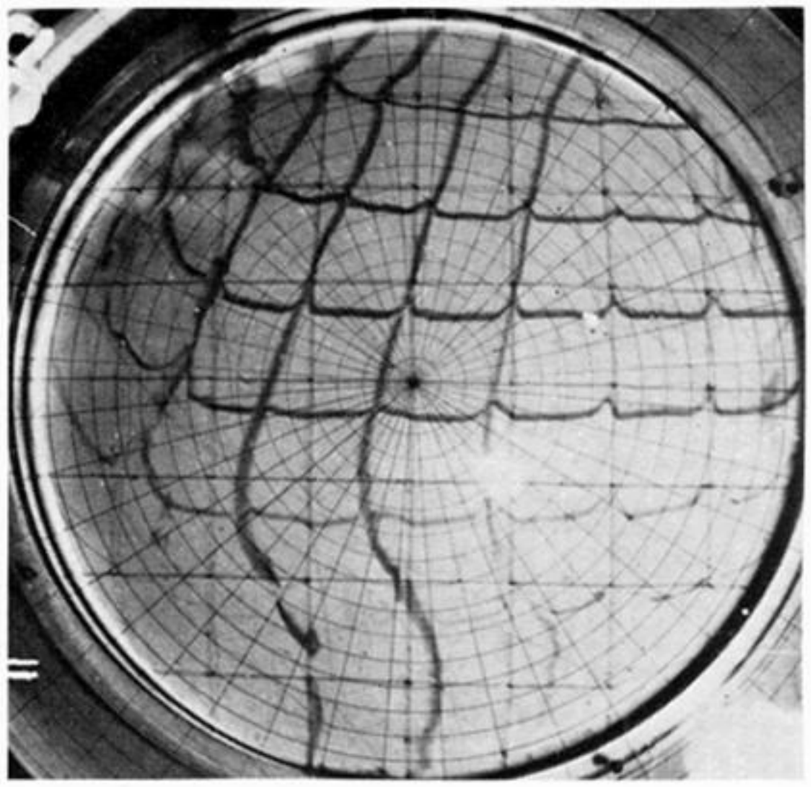

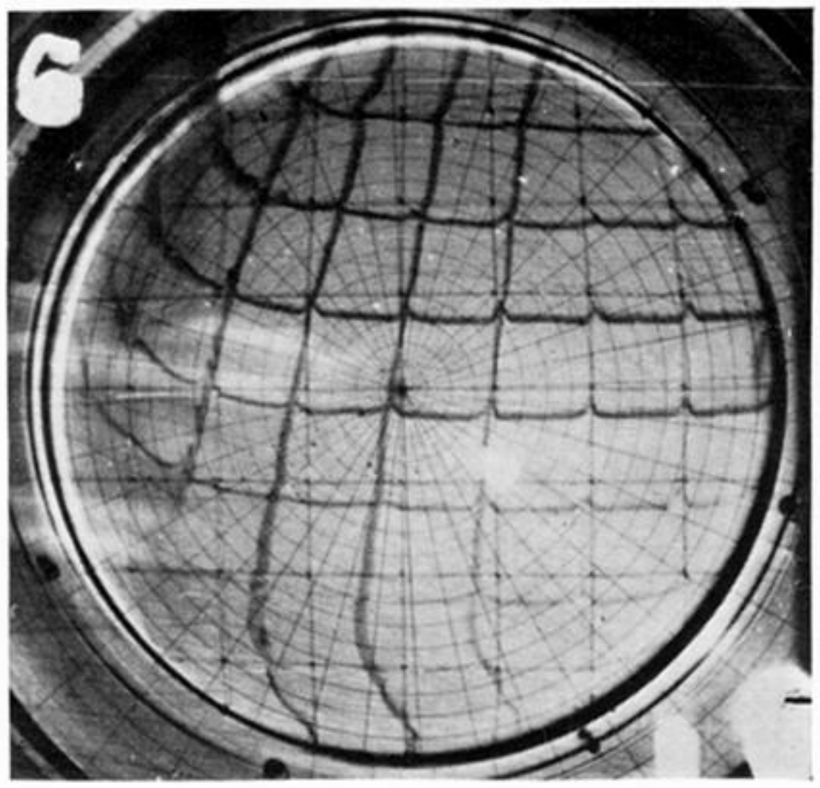

$\epsilon = 0.043$
$\gamma = 0.0070$
$\gamma^{\frac{1}{2}} = 0.084$
$\omega = 0.062\ \text{rad s}^{-1}$
$\Omega = 2.08\ \text{rad s}^{-1}$

$\theta_o = 26°$

← equator

$\epsilon = 0.0075$
$\gamma = 0.0024$
$\gamma^{\frac{1}{2}} = 0.049$
$\omega = 0.031\ \text{rad s}^{-1}$
$\Omega = 6.31\ \text{rad s}^{-1}$

$\theta_o = 31.4°$

equator →

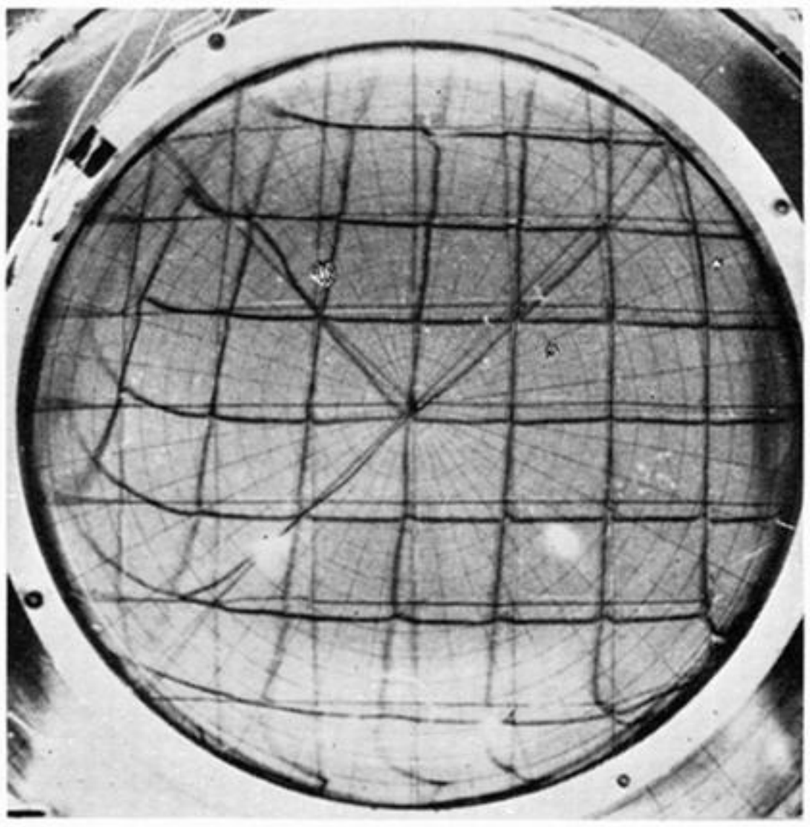

FIGURE 10. Variation in flow pattern as a function of θ_o. The equator and relevant data are indicated for each picture.

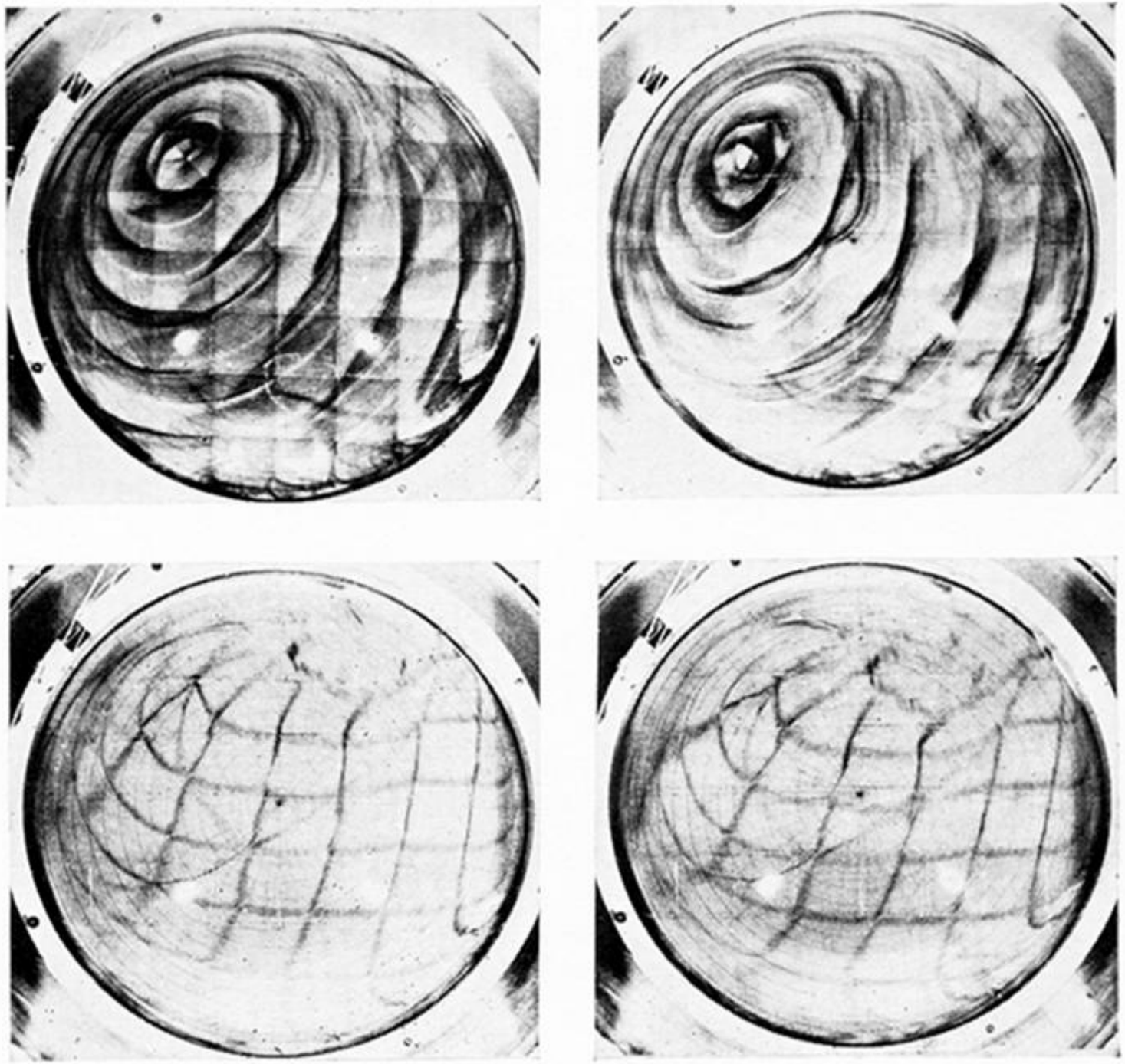

FIGURE 11. Photographs of flow for large ϵ. The right-hand photographs were taken 0.3 s after the left-hand ones. The upper pictures represent a continuous flow of dye; the lower, a pulse. ($\theta_0 = 31.4°$, $\Omega = 6.31$ rad s^{-1}, $\omega = 0.850$ rad s^{-1}, $\epsilon = 0.207$, $\gamma = 0.00245$, $\gamma^{\frac{1}{2}} = 0.0495$.)

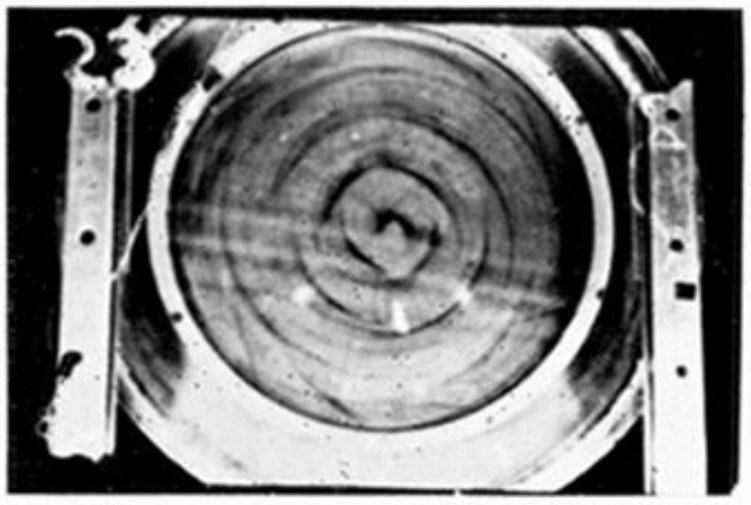

$\Omega = 0$ rad s^{-1}
$\gamma = \epsilon = \infty$

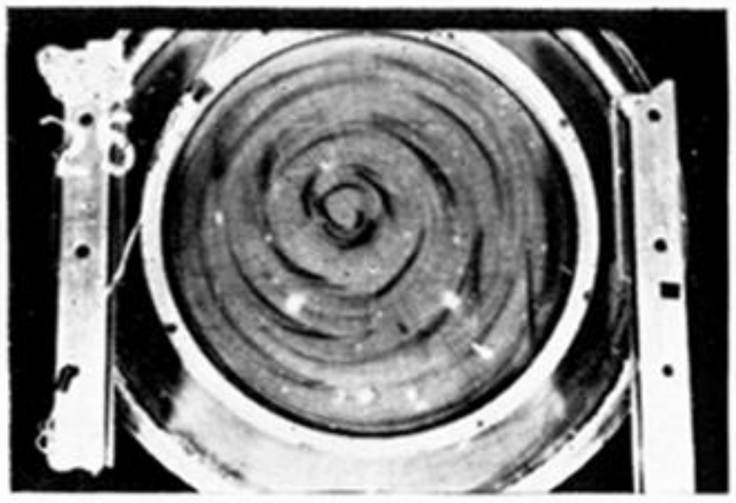

$\Omega = 0.261$ rad s^{-1}
$\gamma = 0.059$
$\gamma^{\frac{1}{2}} = 0.24$
$\epsilon = 0.94$

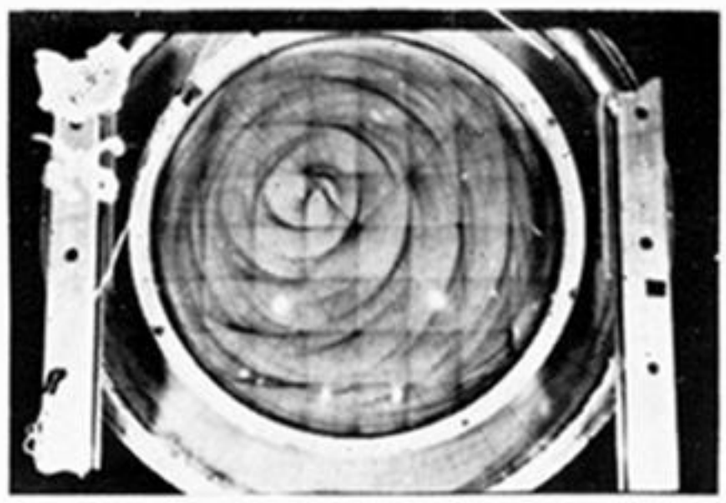

$\Omega = 0.512$ rad s^{-1}
$\gamma = 0.030$
$\gamma^{\frac{1}{2}} = 0.17$
$\epsilon = 0.48$

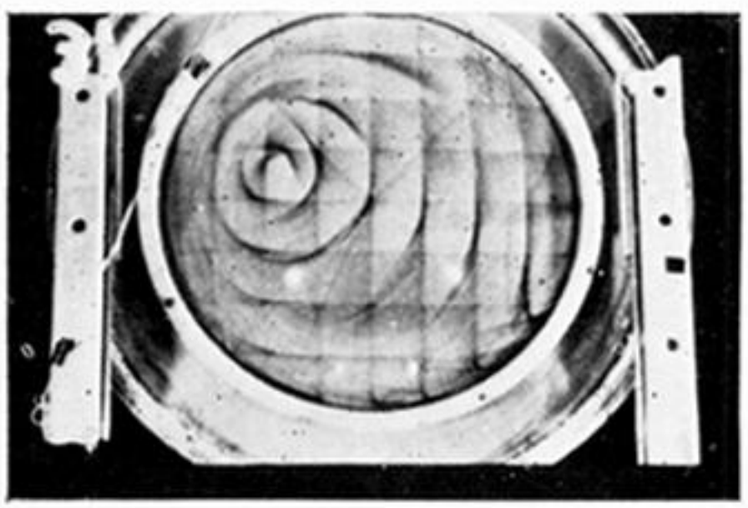

$\Omega = 2.23$ rad s^{-1}
$\gamma = 0.0069$
$\gamma^{\frac{1}{2}} = 0.0831$
$\epsilon = 0.11$

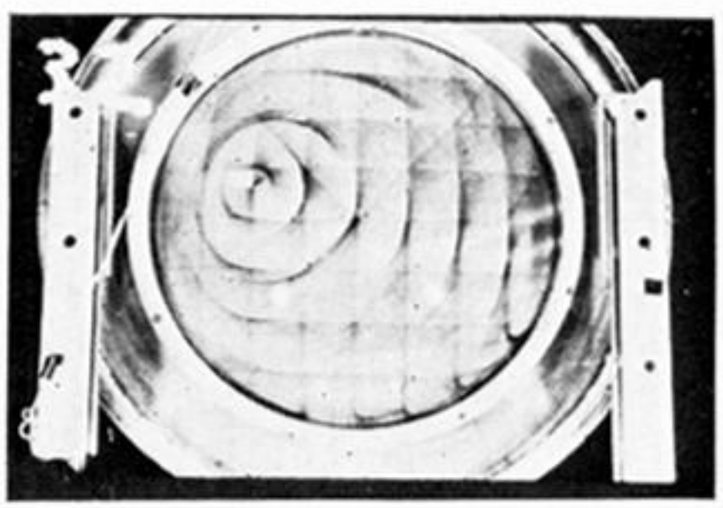

$\Omega = 3.17$ rad s^{-1}
$\gamma = 0.0049$
$\gamma^{\frac{1}{2}} = 0.070$
$\epsilon = 0.077$

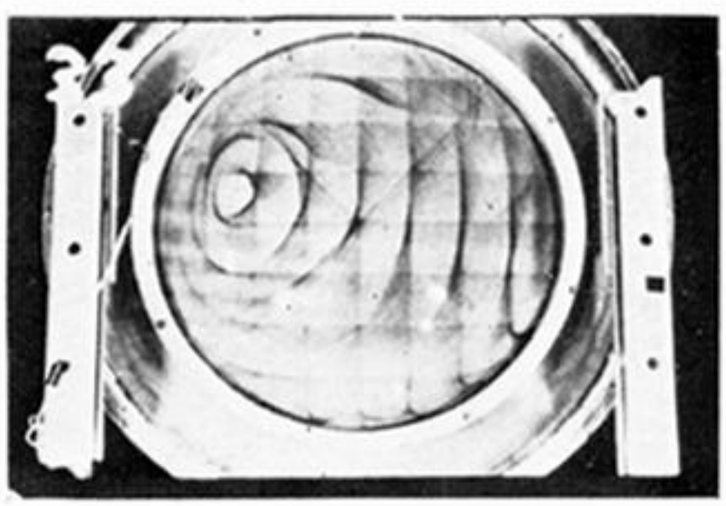

$\Omega = 4.15$ rad s^{-1}
$\gamma = 0.0037$
$\gamma^{\frac{1}{2}} = 0.061$
$\epsilon = 0.059$

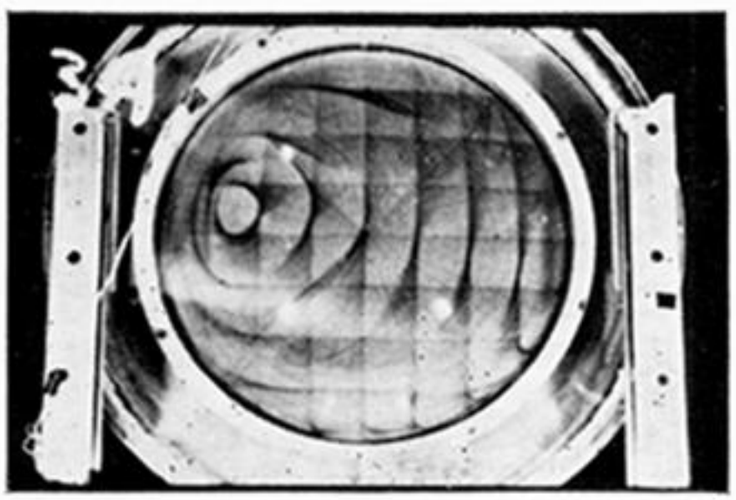

$\Omega = 5.30$ rad s^{-1}
$\gamma = 0.0029$
$\gamma^{\frac{1}{2}} = 0.054$
$\epsilon = 0.046$

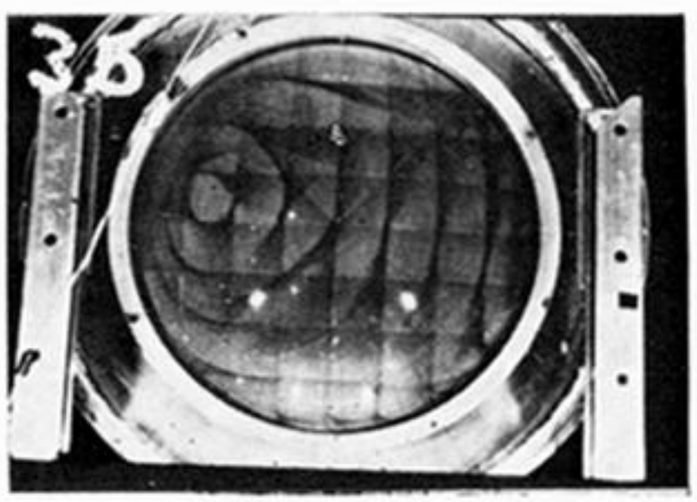

$\Omega = 6.34$ rad s^{-1}
$\gamma = 0.0024$
$\gamma^{\frac{1}{2}} = 0.049$
$\epsilon = 0.039$

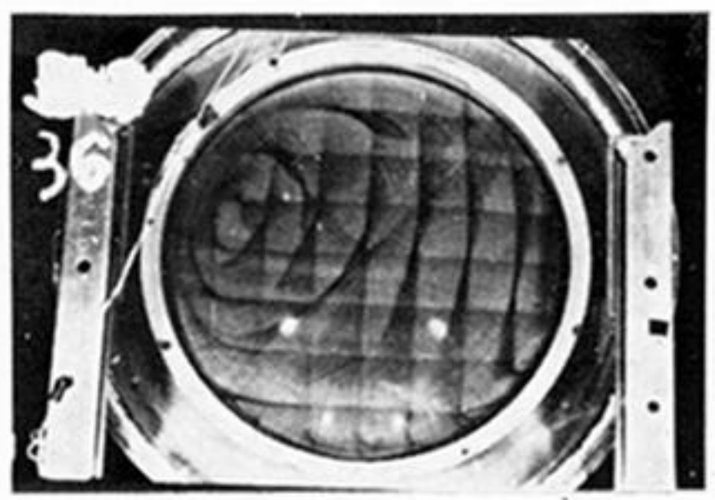

$\Omega = 7.37$ rad s^{-1}
$\gamma = 0.0021$
$\gamma^{\frac{1}{2}} = 0.046$
$\epsilon = 0.033$

FIGURE 12. Flow pattern as a function of Ω ($\theta_o = 31.4°$, $\omega = 0.159$ rad s^{-1}).

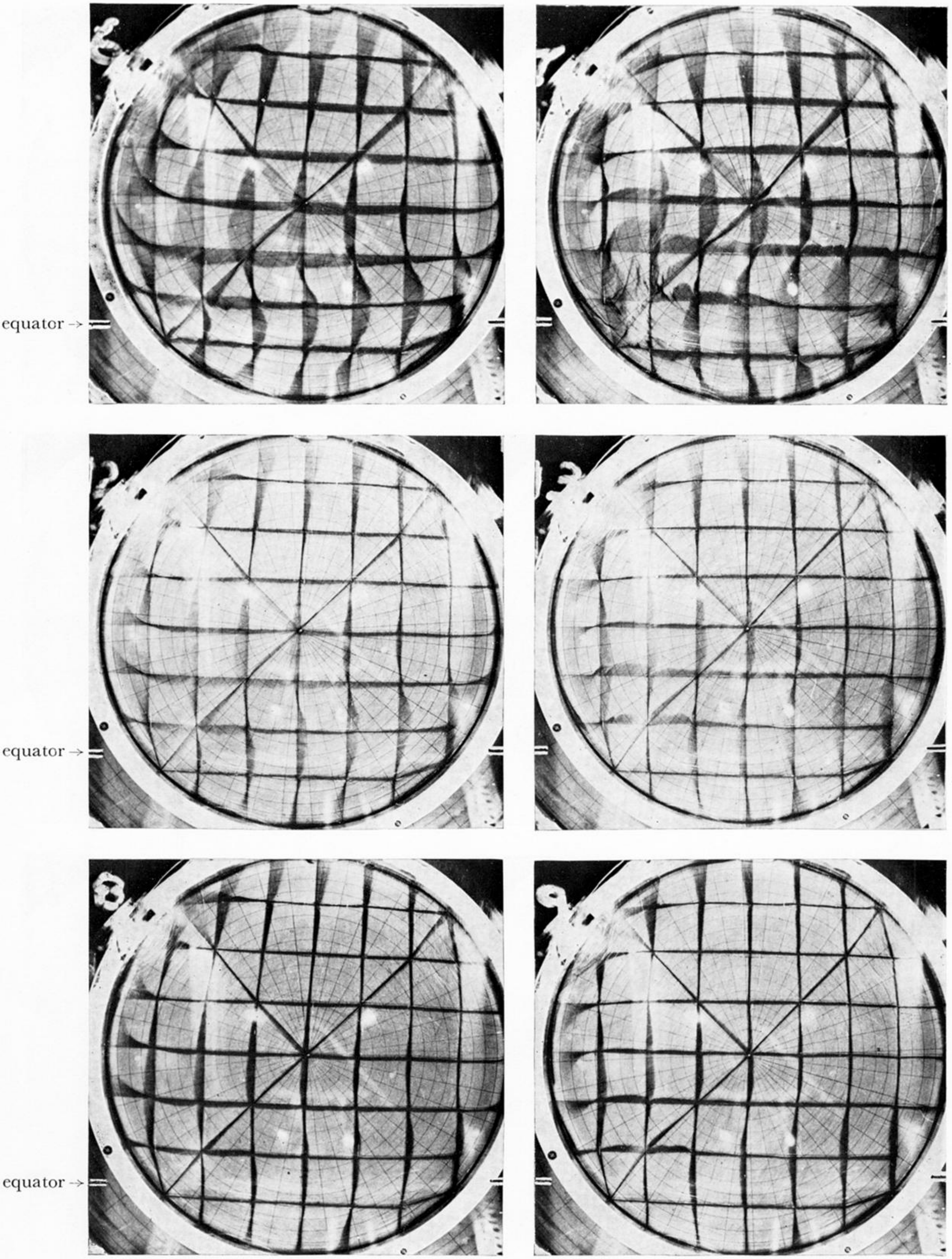

FIGURE 26. Equatorial flow as a function of ω. ($\theta_o = 13.0°$, $\Omega = 6.32$ rad s^{-1}, $\gamma = 0.00214$ for all pictures.) Positive ω appears on the right, negative ω on the left. (*a*) Lower: $\omega = 0.0297$ rad s^{-1}, $\epsilon_{eq} = 0.00392$, $R_{eq} = 0.111$. Centre: $\omega = 0.0994$ rad s^{-1}, $\epsilon_{eq} = 0.0131$, $R_{eq} = 0.372$. Upper: $\omega = 0.249$ rad s^{-1}, $\epsilon_{eq} = 0.0329$, $R_{eq} = 0.931$.

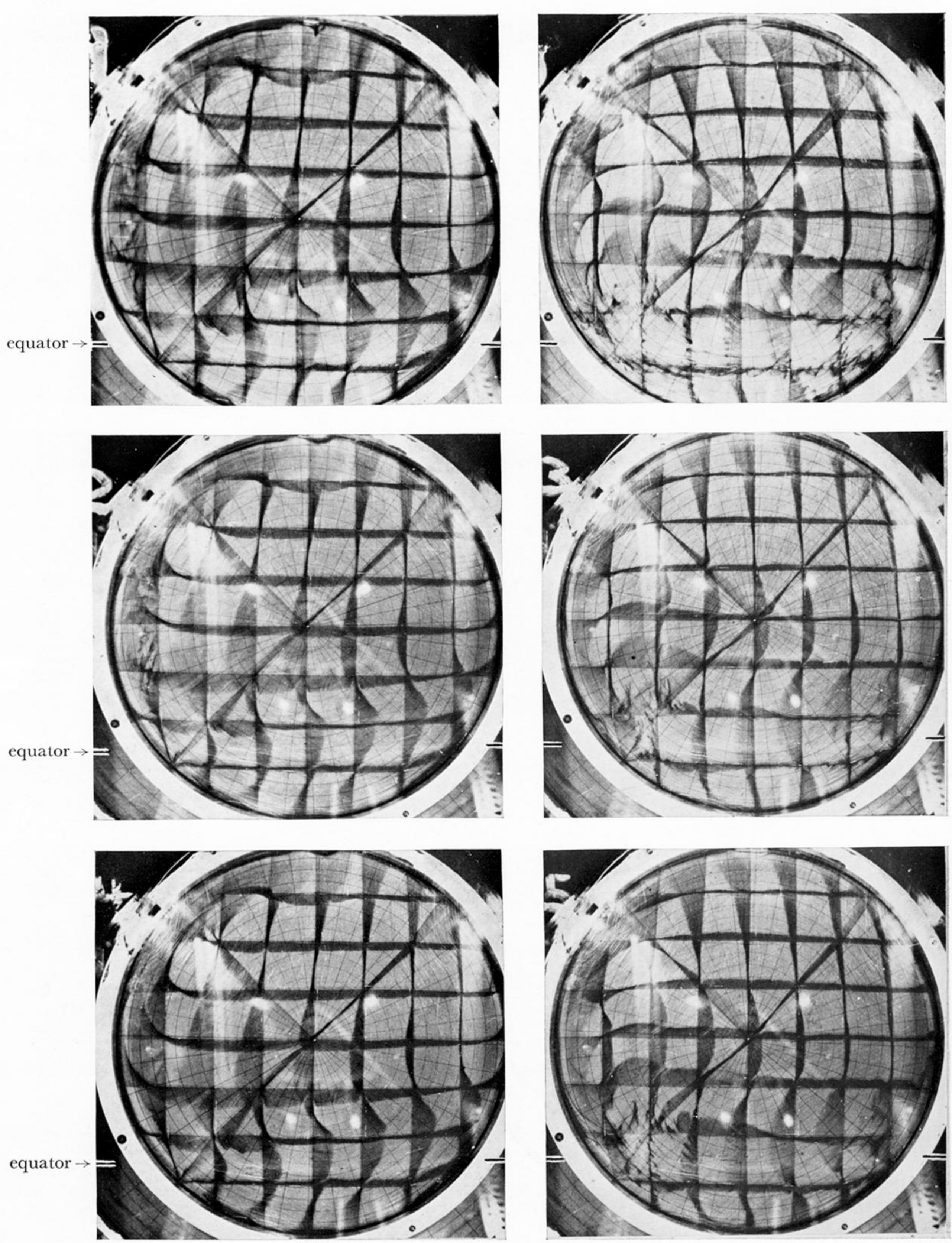

FIGURE 26. (*b*). Lower: $\omega = 0.300$ rad s^{-1}, $\epsilon_{eq} = 0.0396$, $R_{eq} = 1.122$. Centre: $\omega = 0.351$ rad s^{-1}, $\epsilon_{eq} = 0.0463$, $R_{eq} = 1.31$. Upper: $\omega = 0.400$ rad s^{-1}, $\epsilon_{eq} = 0.0528$, $R_{eq} = 1.50$.

equator →

equator →

equator →

FIGURE 26 (*c*). Lower: $\omega = 0.500$ rad s^{-1}, $\epsilon_{eq} = 0.0660$, $R_{eq} = 1.87$. Centre: $\omega = 0.706$ rad s^{-1}, $\epsilon_{eq} = 0.0932$, $R_{eq} = 2.64$. Upper: $\omega = 0.802$ rad s^{-1}, $\epsilon_{eq} = 0.106$, $R_{eq} = 3.00$.

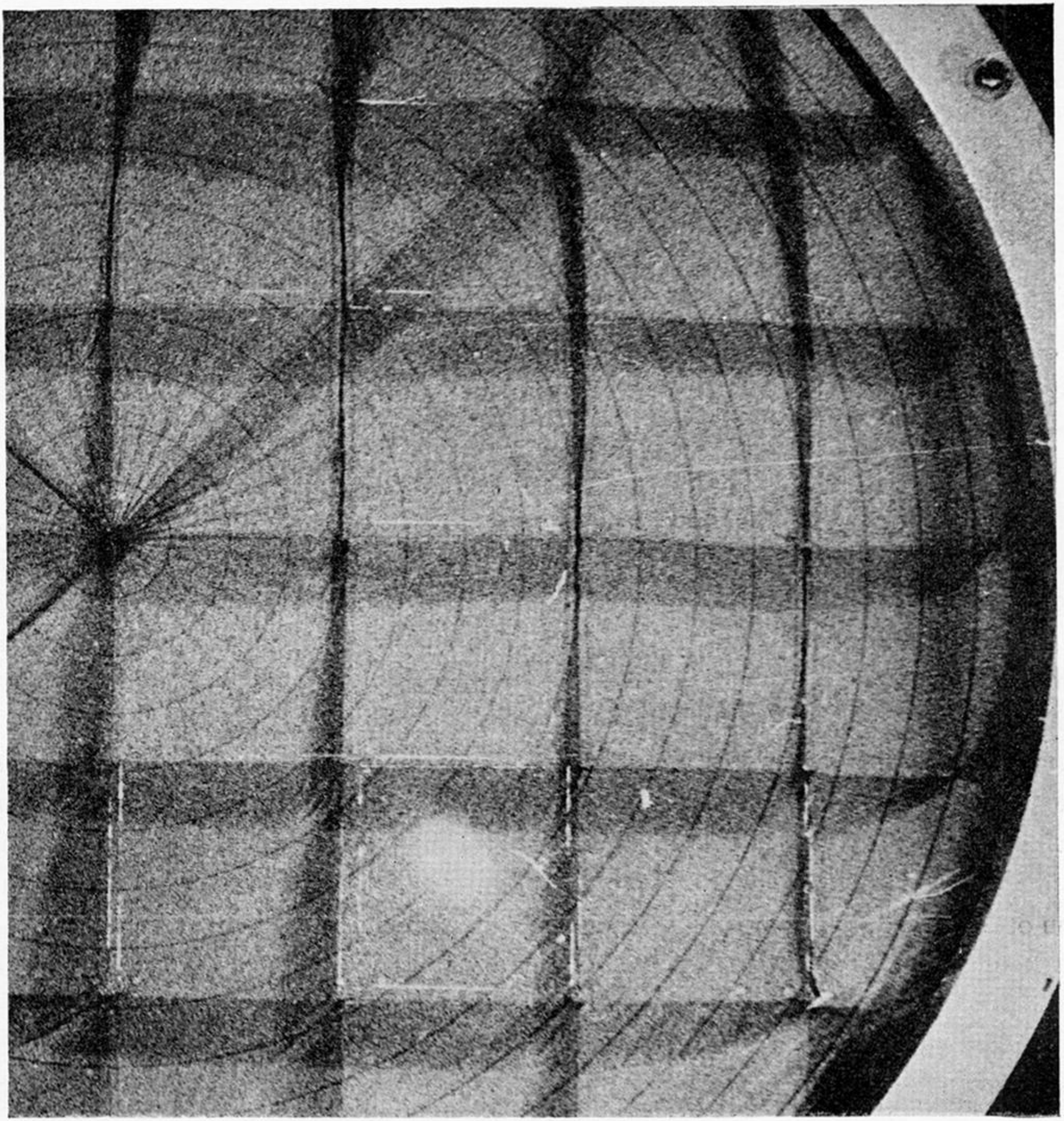

FIGURE 25. Photograph of a northward eastern boundary current (at right centre).
($\theta_0 = 31.4°$, $\epsilon = 0.0260$, $\gamma = 0.00245$, $\gamma^{\frac{1}{2}} = 0.0495$.)